REGENERATION

Conserved stromal EMT program controls regenerative capacity of mesenchymal stromal cells across multiple tissues

Jin-A Kim[1]†, Bong-Woo Park[1]†‡, Hae-Ri Lee[1]†, Gyung-Ah Jung[1], Susie Lee[1], Woo-Sup Sim[2], Hyemi Lee[3], Jihoon Kim[3], Sungho Shin[4], Cheolju Lee[4], Silvia Park[5], Young-Ju Kang[6], Jong-Wook Lee[5], Hee-Je Kim[5], Yunhee Kim Kwon[3], Hun-Jun Park[2,7]*, Il-Hoan Oh[1]*

The regenerative function of stem cells is orchestrated by specialized niches, yet the mechanisms underlying mesenchymal stromal cell (MSC)–mediated support remain unclear. Here, we demonstrate that the epithelial-to-mesenchymal transition (EMT) gradient, together with stemness and pericyte-like properties, is a critical regulator of MSC niche function. High EMT gradients characterize functional MSC subsets that functions as niche supporting hematopoietic stem cells (HSCs), while attenuation of the EMT program impairs HSC support and reproduced in degenerative hematological disorders. Notably, enhancing the EMT program in MSCs (aEMT-MSCs) markedly augments their capacity to promote HSC regeneration and restores defective niches in patients with aplastic anemia. Furthermore, the regenerative effects of aEMT-MSCs extend beyond hematopoiesis to neuronal and cardiovascular tissues, suggesting a conserved niche-supporting program across multiple tissue systems. These findings establish the EMT program as a central regulator of the mesenchymal niche and propose a strategy to address unmet needs in regenerative medicine.

INTRODUCTION

Tissue regeneration is a fundamental biological process essential for maintaining homeostasis and restoring function following injury. This complex process is orchestrated by the coordinated action of tissue-specific stem cells, committed progenitors, and differentiated cells. In the hematopoietic system, hematopoietic stem cells (HSCs) are responsible for the lifelong replenishment and regeneration of blood cells, both under steady-state conditions and in response to stress or transplantation (*1*, *2*). Notably, HSCs exhibit notable heterogeneity in regenerative activity, with distinct states of dormant and actively proliferating subpopulations coexisting in the bone marrow (BM) (*3*). These distinct functional states of HSCs are dynamically regulated, allowing them to switch between quiescence and self-renewal in response to various stimuli, such as BM injury, granulocyte-colony stimulating factor (G-CSF), or interferon-α–induced poly(I:C) (PIPC) production (*2*, *4*).

The dynamic regulation of distinct states of HSC regenerative activity is tightly controlled by the microenvironment, where HSCs engage in complex cross-talk with multiple cell types within the stem cell niche (*5*). These niches are primarily composed of perivascular mesenchymal stromal cells (MSCs) (*6*–*8*), with participation of endothelial cells (ECs) and other cell types (*9*). Mesenchymal cells in the BM exhibit significant heterogeneity, with specific subpopulations identified as key niche components, characterized by the expression of markers such as Nestin (*8*), Prx-1 (*10*), or Leptin receptors (*11*). These perivascular niche cells are characterized by the expression of pericyte markers and are enriched for cells with mesenchymal stem/progenitor properties with colony formation (CFU-F), predominantly localized to the periarteriolar or perisinusoidal regions of the BM (*7*).

Accumulating evidence indicates that the stem cell niche neces§ty to enable coordinated control of hematopoiesis. This dynamic regulation of the microenvironment is critical for maintaining the functional balance between HSC quiescence, self-renewal, and differentiation in response to physiological cues. For instance, during acute myeloid leukemia (AML) or myeloproliferative disorders, mesenchymal niche cells undergo degenerative changes, resulting in compromised support for normal HSCs (*12*, *13*). Similarly, perivascular mesenchymal cells are innervated by the sympathetic nervous system, and adrenergic denervation of the niche leads to a loss of regenerating HSCs and dominance of myeloproliferative neoplastic cells (*14*, *15*). Conversely, stimulation of hematopoiesis induced by 5-fluorouracil (5-FU) treatment causes an adaptive remodeling of BM stromal cells into an activated niche, characterized by the acquisition of stem cell–like properties and phenotypes resembling HSC niche cells (*16*). Similarly, cultured BM MSCs exhibit reversible changes in their HSC-supportive activity when subjected to different culture conditions (*17*), further highlighting the dynamic nature of the stromal niche activity in response to extrinsic cues.

Accordingly, the mechanisms governing the dynamic regulation of niche activity have been highlighted. Several intracellular molecules have been identified as essential components for perivascular

[1]Catholic High-Performance Cell Therapy Center and Department of Medical Life Science, College of Medicine, The Catholic University of Korea, Seocho-gu, Seoul 06591, Republic of Korea. [2]Department of Biomedicine and Health Sciences, The Catholic University of Korea, Seoul 06591, Republic of Korea. [3]Department of Biomedical and Pharmaceutical Sciences, Kyung Hee University, 26 Kyungheedae-ro, Dongdaemun-gu, Seoul 02447, Republic of Korea. [4]Chemical and Biological Integrative Research Center, Korea Institute of Science and Technology, Seoul 02792, Republic of Korea. [5]Catholic Hematology Hospital, Seoul St. Mary's Hospital, College of Medicine, The Catholic University of Korea, Seoul 06591, Republic of Korea. [6]Division of Nonclinical Research, Research Center, RegenInnopharm Inc., Seocho-gu, Seoul 06591, Republic of Korea. [7]Division of Cardiology, Department of Internal Medicine, Uijeonbu St. Mary's Hospital, College of Medicine, The Catholic University of Korea, Uijeonbu 11765, Republic of Korea.
*Corresponding author. Email: iho@catholic.ac.kr (I.-H.O.); cardioman@catholic.ac.kr (H.-J.P.)
†These authors contributed equally to this work.
‡Present address: Department of Biomedical Informatics, College of Applied Life Sciences, Jeju National University, Jeju Special Self-Governing Province 63243, Republic of Korea.

niche cell integrity, with their deficiency leading to myeloproliferative disorders or hematopoietic insufficiency (*18*–*20*). Alternatively, specific combinations of transcription factors, including MEF2C, have been reported to enhance the niche activity of cultured MSCs (*21*). However, despite identification of molecules in the integrity of niche cells, the key cellular parameters that control the dynamic changes in niche activity in response to physiological cues remain to be elucidated.

Notably, our previous research demonstrated that ex vivo cultured MSCs under two-dimensional (2D) or 3D conditions exhibited distinct hematopoietic progenitor cell (HPC)–supporting activities, which were associated with differences in the epithelial-to-mesenchymal transition (EMT) gradient (*22*). However, the possibility that these differences in EMT gradient among MSCs represents a parameter for quantitative differences in niche activity of the MSCs, nor its physiological relevance to dynamic control of niche activity during response to extrinsic stimuli has not been explored.

In the present study, we investigated the role of changes in the EMT gradient and molecular changes in mesenchymal cells during dynamic alterations in niche activity under both normal and pathological conditions. We found that the EMT gradient, coupled with the acquisition of stemness and pericyte-like phenotypes, a stromal EMT program, represents coordinated changes in BM mesenchymal stroma that reflect the dynamic response of the mesenchymal niche to physiological cues for regulating HSC fate. We demonstrate that MSCs engineered with microRNAs (miRNAs) to enhance this EMT program significantly boost the regeneration of multiple tissues, thus pointing to its possibility as a broad-spectrum microenvironment therapy.

RESULTS

Hierarchical difference of EMT gradient in mesenchymal cells

To investigate the physiological significance of the EMT gradient in stem cell niche, we first investigated whether distinct EMT gradients could be observed among heterogeneous mesenchymal cells in the BM microenvironment and whether these differences correlate with their niche activity. To address this, we used a murine model (Nestin–green fluorescent protein mice) in which niche cells were phenotypically identified by the expression of Nestin and platelet-derived growth factor receptor (PDGFRα), while cells negative for these markers contributed solely to osteochondral tissues (Fig. 1A) (*23*). This model system allowed us to compare EMT gradients between functional niche-enriched and niche-poor mesenchymal populations within their BM microenvironment.

Comparative transcriptomic and EMT gradient analyses using public RNA sequencing (RNA-seq) database (GSE61695) and dbEMT (*24*) revealed significant enrichment of EMT-associated genes in niche-enriched cells ($Nestin^+PDGFR\alpha^+$) compared to niche-poor cells ($Nestin^-PDGFR\alpha^-$), with niche cells displaying an overall increase in the expression of EMT-associated genes (Fig. 1B) ($\log_2$ fold change = 1.29 and −0.28 for EMT-associated genes and total transcriptome, respectively; $P < 0.0001$).

Analysis of individual differentially expressed genes (DEGs) revealed significant up-regulation of EMT-promoting signals in niche-enriched cells compared to niche-poor mesenchymal cells (Fig. 1C). Specifically, master EMT-promoting factors (*Snai1*, *Twist1*, *Foxc2*, *Slug*, *Zeb1*, *Zeb2*, *Sox9*, and *Klf8*) (*25*) showed marked up-regulation in niche-enriched cells, while the EMT inhibitor *Foxo3* was down-regulated. Accordingly, *N-cadherin*, a canonical marker for mesenchymal nature in the osteoblastic niche (*26*), demonstrated significant up-regulation, further supporting the enhanced EMT signature in functional niche-enriched cells (Fig. 1D). In addition, mimicking the characteristics of niche cells identified in BM, the niche-enriched cells expressed higher levels of pericyte markers than niche-poor cells, displaying pericyte-like properties in transcriptome (Fig. 1E). These findings indicate a hierarchical organization of the BM mesenchymal niche, under in vivo BM microenvironment, with functional niche-enriched cells exhibiting a higher EMT gradient and pericyte-like properties compared to niche-poor mesenchymal cells.

Having established the correlation in BM microenvironment, we next investigated whether this relationship was reproduced during in vitro stimulation of niche activity. To this end, we examined cultured MSCs under conditions known to enhance their HPC-supportive function. We treated MSCs with two established niche-activating factors: PIPC, a Toll-like receptor 3 agonist, or substance P (sub-P), factors known to enhance the supportive activity of MSCs (*27*, *28*). The enhanced niche activity of treated MSCs was confirmed by coculture experiments, which demonstrated significantly increased expansion of $CD45^+CD34^+CD90^+$ HPCs with engraftment potential (*29*) in the treated MSCs compared to control MSCs (Fig. 1, F and G).

When examined for EMT, these "stimulated" MSCs exhibited significant up-regulation of master EMT regulators, including *SNAI1*, *SLUG*, *ZEB1*, *ZEB2*, and *N-cadherin* (Fig. 1, H and K). Notably, these stimuli also induced a similar induction of pluripotency-related genes (*OCT4*, *NANOG*, and *SOX2*) (Fig. 1, I and L) and pericyte markers (*NESTIN*, *NG2*, *PDGFR*β, and *CD146*) (Fig. 1, J and M) (*30*). These results show that biological stimuli that enhance the supportive activity of MSCs lead to an up-regulation of the EMT gradient, accompanied by an increase in stemness and pericyte marker genes, as a coordinated cellular program to activate the stem cell–supportive activity of MSCs.

Down-shift of EMT program under nonsupportive microenvironment

To establish a functional relationship between EMT gradient and niche activity, we first examined the impact of EMT down-regulation. MSCs were transfected with small interfering RNAs (siRNAs) targeting key EMT-regulating genes (*SNAI1*, *SLUG*, *ZEB1*, and *TWIST1*). This targeted suppression resulted in significantly decreased expression of EMT factors, accompanied by reduced expression of pluripotency-related genes, exhibiting decreased colony-forming progenitor cells (CFU-F) and diminished niche activity, as evidenced by decreased expansion of $CD45^+CD34^+CD90^+$ hematopoietic repopulating cells (Fig. 2, A to D).

Next, to further investigate whether the relationship between EMT gradient and hematopoietic supportive activity is reproduced under in vivo disease condition, we analyzed the BM of patients with AML, where the mesenchymal niche of BM has been shown to undergo degenerative alterations causing selective loss of support on normal HSCs, while sparing the leukemic cells. EMT gradient analysis of MSCs from the BM of patients with AML revealed significant down-regulation of EMT factors and *N-cadherin* expression levels, accompanied by a similar down-regulation of pluripotency-related genes and pericyte markers compared to MSCs from normal

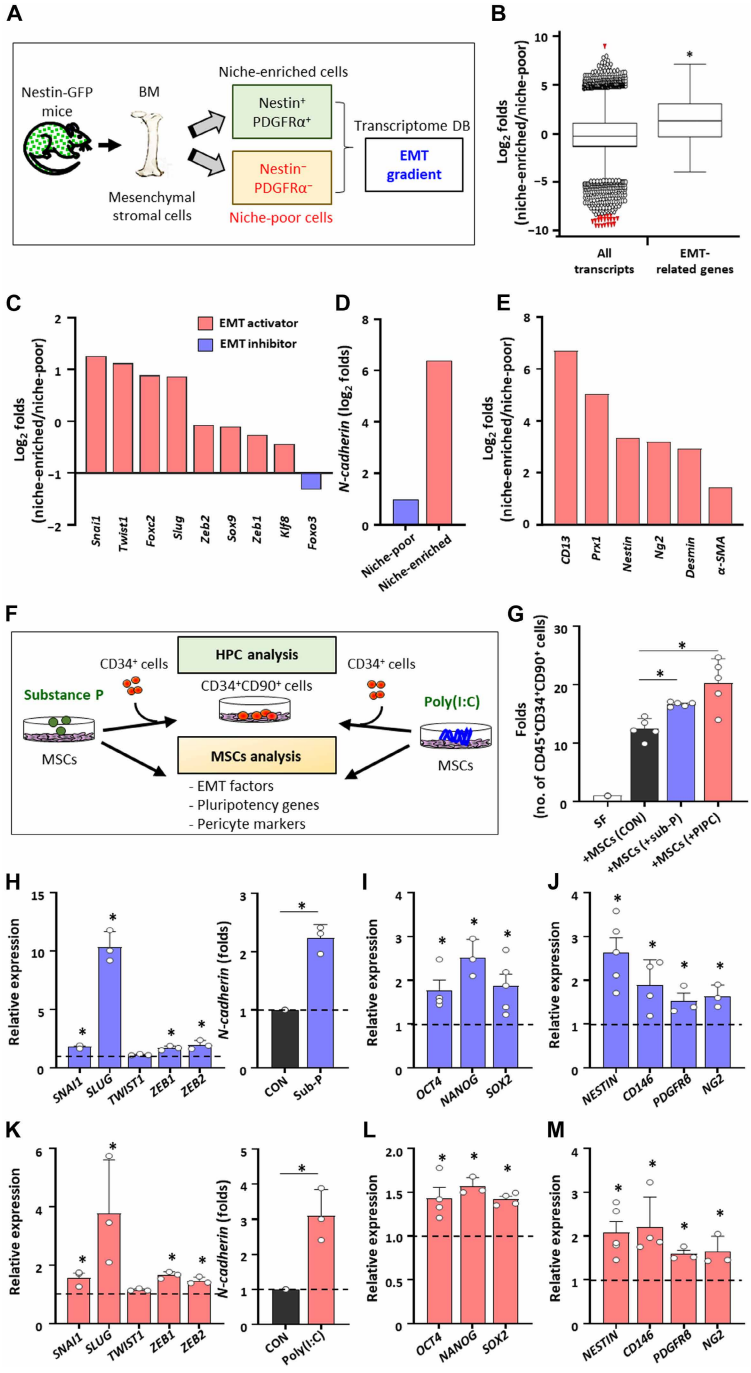

Fig. 1. Increase of EMT gradient in MSCs of higher niche activity. (**A** to **E**) Hierarchical organization of EMT gradient between subsets of BM mesenchymal cells in BM microenvironment. (A) Schematic diagram for analysis. Mesenchymal cell subsets in BM (Nestin^{+}PDGFRα^{+}) contributing to stem cell niche formation (niche-enriched) and those contributing to skeletogenesis, but poor in niche cells (Nestin^{-}PDGFRα^{-}) (niche-poor) were compared for gene expression using public RNA-seq database (GSE61695). (B) Log_2 fold changes of 163 genes annotated in dbEMT between niche-enriched versus niche-poor cells. Expression changes of EMT-related genes were compared to changes of all transcripts. (C and D) Log_2 fold changes of indicated specific genes regulating EMT between niche-enriched and niche-poor cells are shown (C) along with changes in expression level of *N-cadherin* (D). Log_2 fold differences for expression levels of pericyte markers in niche-enriched compared to niche-poor cells (E). (**F** to **M**) EMT gradient program in MSCs stimulated for supporting hematopoiesis. (F) Schematic diagram of the experimental design. MSCs were treated by substance P (sub-P) or poly(I:C) (PIPC) to stimulate hematopoiesis-supporting activities. Resulting expansion of HPCs and associated changes in MSCs were analyzed. (G) Verification of hematopoiesis supporting activities by relative fold expansion of CD45^{+}CD34^{+}CD90^{+} cells after 4 days coculture with control MSCs or stimulated MSCs (sub-P, 10 nM or PIPC, 50 μg/ml) ($n = 5$, one experiment, means ± SEM, $^{*}P < 0.05$). [(H) to (M)] Expression changes of EMT program (EMT, pluripotency, and pericyte marker) in MSCs treated with sub-P [(H) to (J)] or by PIPC [(K) to (M)]. Relative expression levels of EMT factor, pluripotency genes, and pericyte markers in MSCs treated for 3 days with sub-P or PIPC ($n = 3$ to 5, three experiments, means ± SEM, $^{*}P < 0.05$, for each group, respectively).

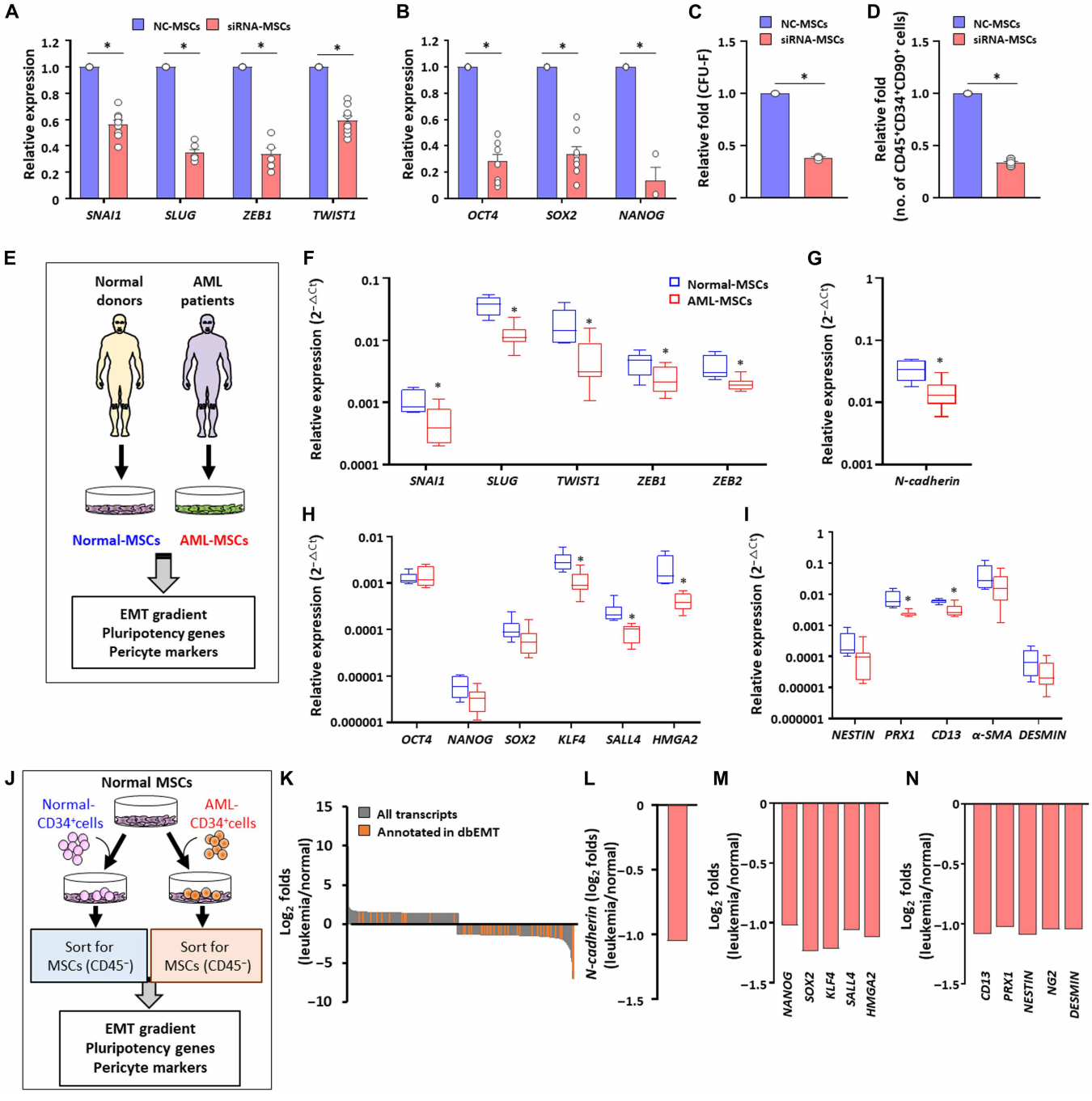

Fig. 2. Lower EMT gradient in the MSCs of decreased niche activity. (**A** to **D**) Influence of down-regulating EMT factors on niche program of MSCs. (A) Knock-down of EMT genes (EMT-KD) in MSCs by mixture of siRNA against EMT factors (siSNAI1, siSLUG, siZEB1, and siTWIST1). (B) Relative expression of pluripotency genes in EMT-KD MSCs (siRNA-MSCs) compared to control MSC (NC-MSCs). (C) Relative CFU-F frequency in EMT-KD MSCs compared to control. (D) Comparing ex vivo expansion folds of $CD45^+CD34^+CD90^+$ cells during 4 days coculture on EMT-KD or control MSCs ($n = 6$ to 9, three experiments, means ± SEM, $^*P < 0.05$). (**E** to **I**) Comparisons of MSCs from normal donors and AML-BM. (E) Schematic representation of comparative analysis of MSCs derived from BM of normal donors or patients with AML. (F to I) Comparisons of expression levels for EMT factor (F), *N-cadherin* (G), pluripotency genes (H), and pericyte markers (I) in normal-MSCs and AML-MSCs. Expression levels of each indicated genes were analyzed by reverse transcription polymerase chain reaction (RT-PCR). The expression levels of each indicated mRNAs relative to the level of 18*S* rRNA ($2^{-\Delta Ct}$) ($n = 6$ for normal donor MSCs, $n = 9$ for MSCs of patients with AML). (**J**) Schematics of the comparative analysis of expression changes in MSCs induced by coculture with normal or AML-derived $CD34^+$ cells. MSCs from normal donors were cocultured with $CD34^+$ cells from normal donors or patients with AML for 5 days, followed by sort purification of MSCs ($CD45^-$) for gene expression analysis. (**K**) Comparisons of EMT related genes and all transcriptomes in MSCs cocultured with normal or leukemic $CD34^+$ cells. (**L** to **N**) Relative expression of *N-cadherin* (L), pluripotency genes (M), and pericyte markers (N) in MSCs cocultured with leukemia $CD34^+$ cells compared to MSCs with normal $CD34^+$ cells.

donors, revealing the changes in opposite direction to that observed in "stimulated" MSCs (Fig. 2, E to I) (*12*, *13*, *31*).

To determine whether leukemic cells directly induce these niche alterations, MSCs were exposed to normal or leukemic CD34$^+$ cells derived from leukemia patients and examined their transcriptomic changes (Fig. 2J). Analysis revealed predominant down-regulation of EMT-related genes following exposure to leukemic blast cells; specifically, among the 42 DEGs ($P < 0.05$) matched to dbEMT, 30 genes were down-regulated and 12 genes were up-regulated (Fig. 2K). Similarly, decreased *N-cadherin* expression and down-regulation of stemness genes (*NANOG*, *SOX2*, *KLF4*, *SALL4*, and *HMGA2*) and pericyte markers (*CD13*, *PRX1*, *NESTIN*, *NG2*, and *DESMIN*) were observed together (Fig. 2, L to N). These findings indicate that leukemic blasts directly cause a shift in the "EMT gradient program" reproducing the changes observed in the mesenchymal cells in the BM of patients with AML. Collectively, these results demonstrate that changes in the EMT gradient program in MSCs represent a microenvironmental parameter for stem cell–supportive activity, which is adaptively modulated by extrinsic signals from regenerative or degenerative cues in the microenvironment (fig. S1)

Establishment of MSCs coaxed for enhanced EMT program

Based on the role of EMT gradients in niche function, we developed an approach to engineer MSCs with increase of EMT gradient for enhanced regenerative capacity. Considering the key role of miRNAs in controlling cell fate changes, including the EMT gradient (*22*, *32*), we screened miRNAs that can simultaneously enhance the EMT gradient and stemness in MSCs through bioinformatics analysis using the miRNA database (miRTarBase and TargetScan). We identified miRNAs (miR-124-3p and miR-203-3p) that can target EMT factors (*SNAI1*, *SLUG*, *ZEB1*, and *ZEB2*) and miRNAs (miR-34a-5p, miR-128-3p, and miR-145-5p) that can regulate stemness-related genes (*OCT4*, *SOX2*, *KLF4*, and *NANOG*) (fig. S2A).

Following various functional screening on the effects of antisense oligonucleotide (ASOs) on cellular proliferation, colony formation, and differentiation of MSCs (fig. S2, B to D) and screening by coculture with hematopoietic cells (fig. S3), we chose a combination of ASOs against miR-124-3p/miR-145-5p, which exhibited higher capacity to generate CD34$^+$ hematopoietic progenitors in recipient mice BM than other combinations in the test for supporting HPCs (fig. S3D). MSCs transfected with ASOs against miR-124-3p and miR-145-5p exhibited significant down-regulation of miR-124-3p and miR-145-5p (Fig. 3A). Moreover, these cells exhibited up-regulation of genes related to stemness (*SOX2*, *OCT4*, *NANOG*, and *KLF4*), EMT (*SNAI1*, *SLUG*, and *ZEB1*), and pericyte markers (*NESTIN*, *PDGFR*α, and *CD146*) (Fig. 3, B to E), thus reproducing the characteristics of the EMT-activated stimulatory mesenchymal niche (aEMT-MSC).

Transcriptomic analysis of these aEMT-MSCs demonstrated a distinctive transcriptome profile, conserved across various MSC batches yet divergent from MSCs subjected to control transfection (fig. S4, A and B). Gene ontology analysis of the DEGs ($P < 0.05$) revealed significant enrichment of molecules involved in cellular responses to external stimuli, cell communication, and cellular signaling (fig. S4C).

Proteomic analysis via liquid chromatography–tandem mass spectrometry (LC-MS/MS) identified 316 differentially expressed proteins ($P < 0.05$) as targets of miR-124-3p or miR-145-5p (fig. S5A).

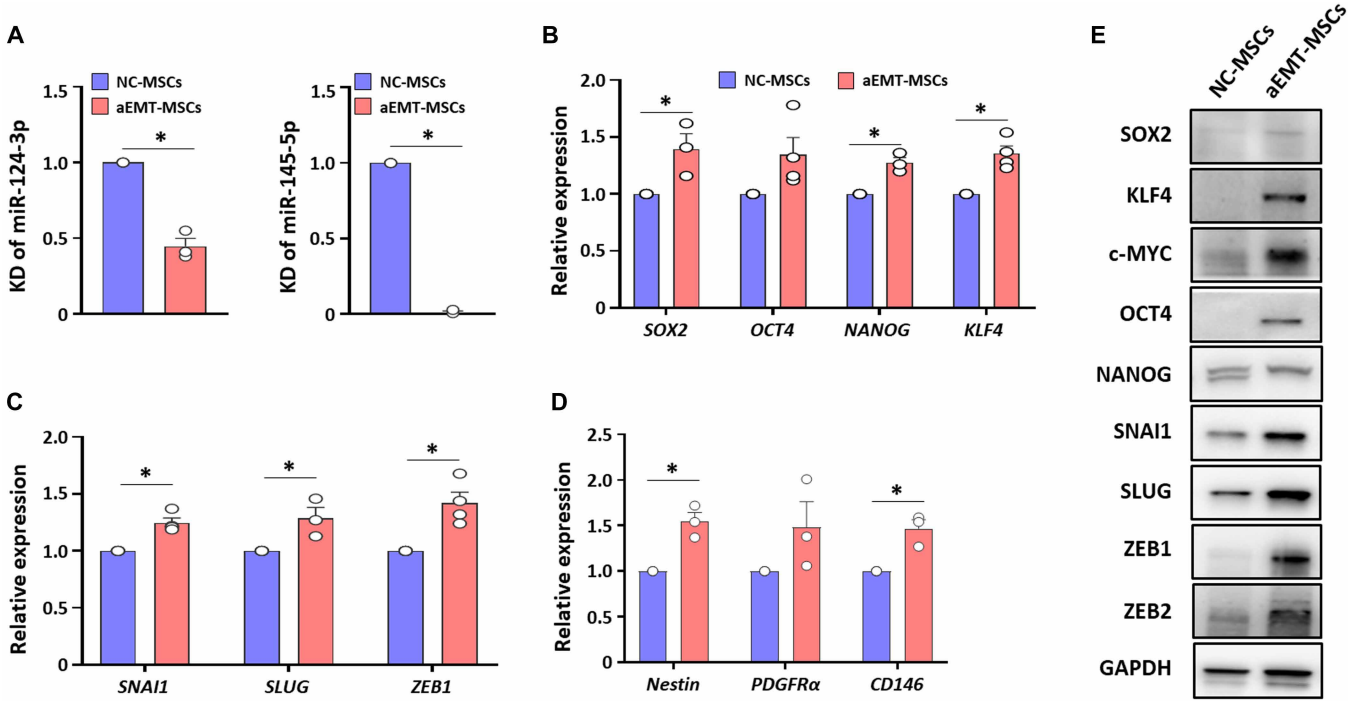

Fig. 3. Characterization of EMT-activated MSCs induced by ASOs inhibiting miR-145-5p and miR-124-3p. (**A**) KD of miR-124-3p and miR-145-5p in for EMT activation (aEMT-MSCs) compared to negative control (NC)-MSCs ($n = 3$, means ± SEM, $^*P < 0.05$). (**B** to **D**) Comparisons for expression changes of pluripotency genes (*SOX2*, *OCT4*, *NANOG*, and *KLF4*) (B), EMT factors (*SNAI1*, *SLUG*, and *ZEB1*) (C), and pericyte markers (*NESTIN*, *PDGFR*α, and *CD146*) (D) between aEMT-MSCs and NC-MSCs ($n = 3$, means ± SEM, $^*P < 0.05$). (**E**) Western blot analysis for expression changes of each indicated genes at protein levels between aEMT-MSCs and NC-MSCs.

Upstream pathway analysis of these 316 proteins using ingenuity pathway analysis revealed that the pathways anticipated to be upregulated in aEMT-MSCs were predominantly enriched for those involved in stemness, tissue regeneration, or EMT progression, including PCGEM1 (*33*), HIF1A (*34*), NFE2L2 (*35*), ERBB2 (*36*), MAPK9 (*37*), CCL5 (*38*), NCOA3 (*39*), GLI (*40*), and FOXM1 (*41*, *42*). On the other hand, the analyses of pathways predicted to be inhibited were those for suppression of regeneration and EMT, including let-7 (*43*), miR-122 (*44*), or CST5 (fig. S5B) (*45*). Together, the aEMT-MSCs coaxed by ASOs against miR-124-3p/miR-145-5p successfully recapitulated the elevated EMT gradient program observed in endogenous MSCs exposed to regenerative stimuli and exhibited molecular signature involved in regenerative signaling pathways.

aEMT-MSCs promote self-renewal of normal HSCs

To evaluate the potential of aEMT-MSCs as an approach to boost regeneration, we first investigated their capacity to support HSC self-renewal and expansion (Fig. 4A). Coculturing $CD34^+$ cells with aEMT-MSCs resulted in significantly greater expansion of hematopoietic progenitors compared to stroma-free conditions or coculture with control MSCs (Fig. 4, B to D), indicating that aEMT-MSCs provide a more supportive niche for ex vivo expansion of HPCs.

To evaluate the in vivo regenerative potential of the cocultured hematopoietic cells, we transplanted them into immunocompromised mice. The transplantation of cells cocultured with aEMT-MSCs resulted in significantly enhanced engraftment of human hematopoietic cells and their primitive subsets ($CD45^+CD34^+$ and $CD45^+CD34^+CD38^-$) compared to the control MSC group (8.4- and 16.3-fold, respectively; $^*P < 0.05$), suggesting that aEMT-MSCs provide a microenvironment that supports the expansion of hematopoietic progenitors with enhanced capacity for in vivo regeneration of HSCs (Fig. 4, E to G).

To quantitatively assess the regeneration of HSCs in recipient BM, we performed a competitive repopulating unit (CRU) analysis (*46*). This assay determines the frequency of HSCs capable of repopulating ablated BM by transplanting limiting doses of primary recipient BM into secondary recipients. This limiting dilution analysis demonstrated that hematopoietic cells cocultured with aEMT-MSCs produced significantly higher numbers of CRUs than control MSCs (14.8- versus 1.39-fold, respectively; $P < 0.0$, confirming the enhanced capacity of aEMT-MSCs to support the regeneration/self-renewal of long-term repopulating HSCs (Fig. 4, H and I).

Notably, these enhanced hematopoiesis-supporting effects of aEMT-MSCs were similarly observed in the cotransplantation model, exhibiting higher engraftment of human $CD34^+$ cells in the coinjection with aEMT-MSCs than with negative control (NC)–MSCs (fig. S6), but without clonal bias of engrafted hematopoietic cells or stimulation of leukemic cells (fig. S7). These findings suggested its potential for translational application of aEMT-MSCs for facilitation of hematopoiesis without the risk of promoting the leukemogenic process. Together, these findings demonstrate that aEMT-MSCs, generated by activating the EMT gradient program, exhibit enhanced HSC-supportive properties, resulting in increased regeneration of long-term repopulating HSCs compared to control MSCs.

Activation of EMT program reverts niche defects in hematological disease

Having demonstrated the enhanced HSC-supportive functions of aEMT-MSCs under normal conditions, we next investigated whether they could exert similar effects on HSCs in the context of hematological diseases, such as aplastic anemia (AA), a degenerative disorder characterized by pancytopenia and hematological insufficiency. Investigation of the bone marrow of AA patients revealed pancytopenia in all hematopoietic lineages, including colonogenic cells (CFC), megakaryocytic progenitors (CFU-MK), and hematopoietic progenitor cells (fig. S8), indicating a defective hematopoiesis.

When analyzed for mesenchymal progenitors, the BM of patients with AA exhibited markedly lower numbers of CFU-F, with 53% of the 36 BM samples from patients with AA failing to produce any CFU-F (fig. S9, A and B). The remaining 47% of the samples that managed to form colonies and proliferate in culture, referred to as AA-MSCs, tended to exhibit lower expression levels of *SNAI1*, *SLUG*, *TWIST1*, and *ZEB1* than MSCs from normal donors (Fig. 5A). When cocultured with normal $CD34^+$ cells, these AA-MSCs exhibited significantly lower support than normal MSCs for the expansion of hematopoietic progenitors ($CD45^+CD34^+$ and $CD45^+CD34^+CD90^+$), suggesting a defect in mesenchymal support in AA (Fig. 5, B to D).

To determine whether these mesenchymal niche defects can be rescued by increasing the EMT gradient, we transfected AA-MSCs with ASOs against miR-124-3p/miR-145-5p (AA-MSC + EMT) and examined for their HSC-supportive activities. EMT activation in AA-MSCs significantly enhanced their stem cell–supportive activities, leading to a substantial increase in the expansion of hematopoietic cells and progenitors ($CD45^+CD34^+CD90^+$ cells) compared to scrambled control MSCs (Fig. 5, E to H). Notably, the magnitude of hematopoietic progenitor expansion enhanced by EMT activation was comparable between AA-MSCs and normal MSCs (2.1- versus 1.8-fold for $CD45^+$ cells, 2.5- versus 2.2-fold for $CD45^+CD34^+$ cells, and 4.1- versus 4.0-fold for $CD45^+CD34^+CD90^+$ cells, respectively), indicating that EMT activation restored niche activity in AA-MSCs (Fig. 5I). Similarly, the clonogenic potential of MSCs from patients with AA was significantly enhanced by increasing the EMT gradient (fig. S10A). These findings suggest that the defective niche activity in AA-MSCs could, at least in part, originate from a lower EMT gradient, and increasing these EMT gradients can reboost their stem cell–supportive activity for recovery from hematological insufficiency in AA. Moreover, the primitive hematopoietic subsets from patients with AA were significantly expanded by aEMT-MSCs (fig. S10, B to D), thus showing that the hematopoietic progenitors of patients with AA retain the potential to be expanded by aEMT-MSCs.

EMT-activated MSCs serve as microenvironment for nonhematological tissues

Given the enhanced stem cell–supportive properties of aEMT-MSCs and their similarity to pericytes in multiple tissue types (*47*), we hypothesized that the regenerative potential of aEMT-MSCs might extend beyond the hematopoietic system. To test this hypothesis, we first examined the effects of aEMT-MSCs on neuronal progenitor cells (NPCs), based on previous studies on the cellular interaction and protective effects of MSCs on NPCs (*48*). Coculture of EMT-activated MSCs with TERT-immortalized NPCs resulted in a significant increase in neurosphere formation (Fig. 6A). Quantitative measurement by limiting dilution showed a significantly increased frequency of neurosphere-forming cells in the EMT-MSC cocultures compared to control MSCs, indicating enhanced NPC self-renewal (Fig. 6B). Moreover, NPCs cocultured with aEMT-MSCs exhibited increased expression of NPC-related

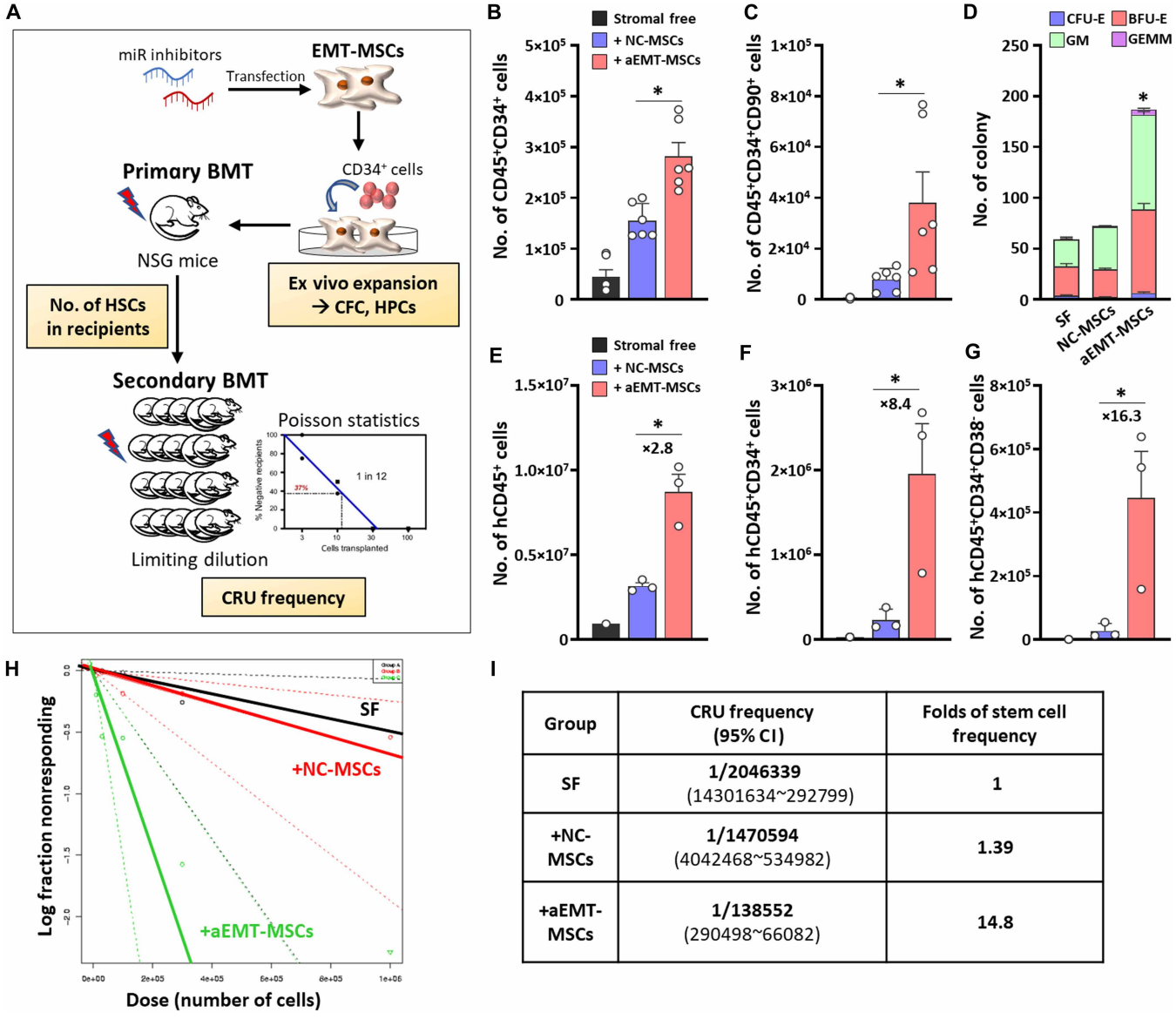

Group	CRU frequency (95% CI)	Folds of stem cell frequency
SF	1/2046339 (14301634~292799)	1
+NC-MSCs	1/1470594 (4042468~534982)	1.39
+aEMT-MSCs	1/138552 (290498~66082)	14.8

Fig. 4. Enhancement of HSC regeneration by EMT-activated MSCs. (**A**) Experimental design. EMT-activated MSCs (aEMT-MSCs) were prepared by cotransfection of MSCs with ASOs inhibiting miR-124-3p and miR-145-5p. $CD34^+$ cells were cocultured with NC-MSCs or aEMT-MSCs or in stroma-free (SF) condition for 4 days and analyzed for hematopoietic regeneration at 16 weeks posttransplantation assessed by expansion of hematopoietic progenitors or self-renewal of in vivo repopulating HSCs. HSC self-renewal was analyzed by engraftment in primary recipient BM and transplantation into secondary recipient mice for limiting dilution analysis to calculate CRU frequency in each group. (**B** to **D**) Ex vivo expansion of hematopoietic progenitors assessed by numbers of $CD45^+CD34^+$ (B), $CD45^+CD34^+CD90^+$ cells (C), and colony-forming cells (D) ($n = 6$, three experiments, means ± SEM, $^*P < 0.05$). (**E** to **G**) Engraftment of HSCs in primary recipients analyzed by total numbers of human hematopoietic cells (E), $CD45^+CD34^+$ cells (F), and $hCD45^+CD34^+CD38^-$ cells (G) in each recipient BM. ($n = 3$, one experiment, means ± SEM, $^*P < 0.05$). Fold differences in numbers in aEMT-MSCs group relative to NC-MSCs groups are numerically labeled. (**H** and **I**) Difference in regenerated HSC numbers by CRU analysis. Frequencies of CRUs that can repopulate recipient BM were measured by Poisson statistics on limiting dilution transplantation into secondary mice. Shown are the limiting dilution analysis profile (H) and fold CRU frequency on each group MSC coculture relative to the serum free conditions (I) ($n = 5$, means ± SEM, $^*P < 0.05$). CI, confidence interval.

genes (*NESTIN*, *MSI1*, and *SOX2*) and, upon differentiation, significantly higher numbers of undifferentiated neural progenitors ($Nestin^+$ and $NG2^+Nestin^+$) and immature neuronal cells ($Tuj1^+Nestin^+$) compared to control MSCs (Fig. 6, C and D).

To investigate the in vivo effects of aEMT-MSCs on neuronal regeneration, we used a neurotoxic injury model induced by ibotenic acid (IBO) injection into the entorhinal cortex, resulting in damage to dentate gyrus granular cells and pyramidal cells (*49*). Transplantation of aEMT-MSCs into the hippocampus significantly increased the proliferation of NPC ($BrdU^+Sox2^+$) and intermediately differentiated neuronal cells ($BrdU^+Tuj1^+$) in the subgranular zone (SGZ) and granular cell layer (GCL) of the hippocampus, the neurogenic loci of adult brain (*50*), at 4 weeks postinjection (Fig. 6, E to H, and fig. S11). Long-term follow-up at 8 weeks showed an increase in mature neuronal populations ($NeuN^+BrdU^+$) and a total increase in $BrdU^+$ cells in transplanted brain region (fig. S12). These

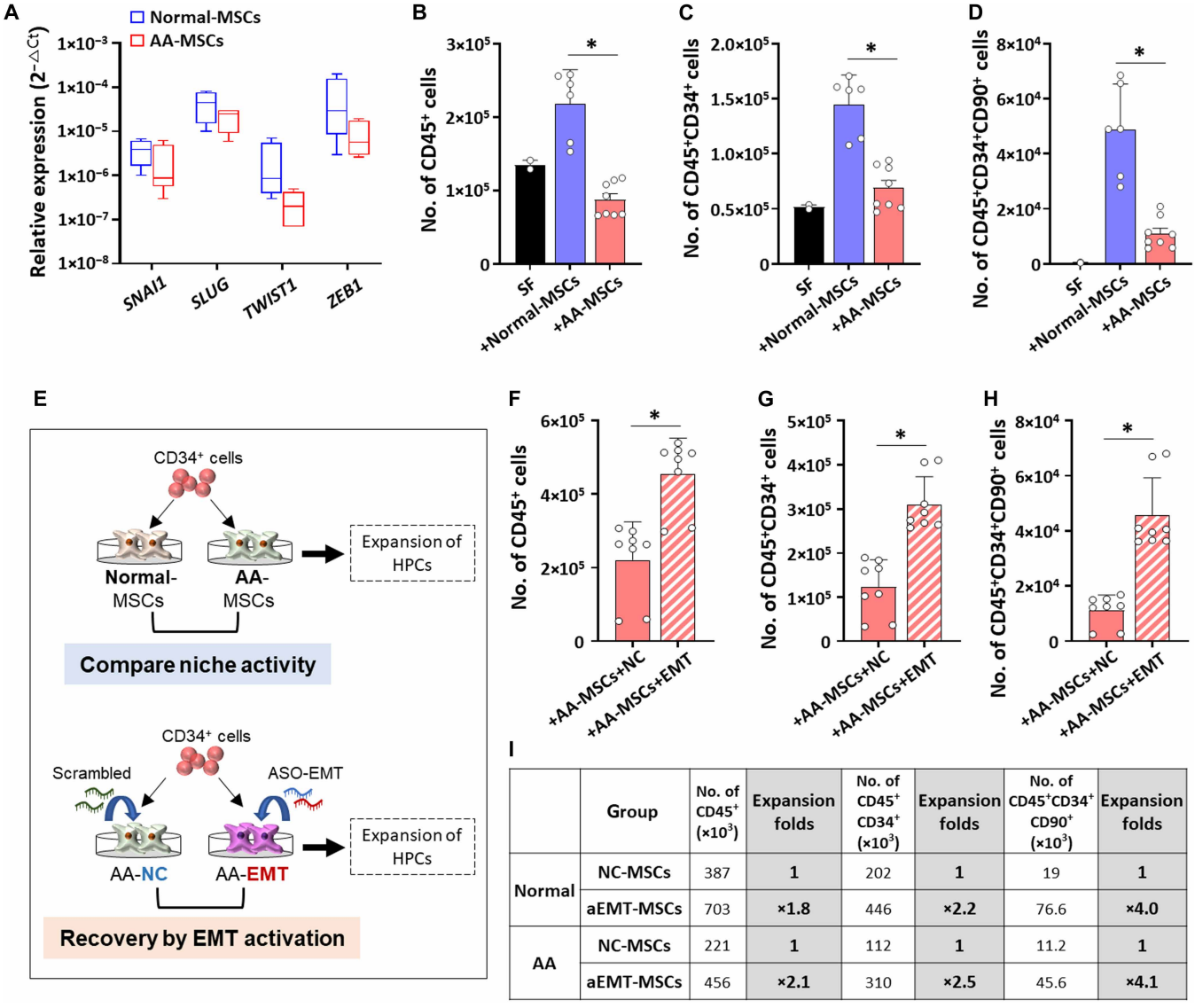

	Group	No. of CD45+ (×10^3)	Expansion folds	No. of CD45+ CD34+ (×10^3)	Expansion folds	No. of CD45+CD34+ CD90+ (×10^3)	Expansion folds
Normal	NC-MSCs	387	1	202	1	19	1
	aEMT-MSCs	703	×1.8	446	×2.2	76.6	×4.0
AA	NC-MSCs	221	1	112	1	11.2	1
	aEMT-MSCs	456	×2.1	310	×2.5	45.6	×4.1

Fig. 5. Restoration of defective niche in AA by EMT-activated MSCs. (**A**) Comparisons for expression levels of EMT factors between culture-expanded AA and normal MSCs by RT-PCR. The expression levels of each indicated mRNAs for EMT factors relative to the level of 18*S* rRNA ($2^{-\Delta Ct}$) ($n = 4$ for normal donor MSCs, $n = 6$ for MSCs of patients with AA). (**B** to **D**) Comparisons for HPC-supporting capacity of normal and AA-MSCs, determined by numbers of total $CD45^+$ cells (B), $CD45^+CD34^+$ cells (C), and $CD45^+CD34^+CD90^+$ cells (D) after coculture under each condition for 4 days ($n = 6$ from three normal donor MSCs, $n = 8$ from four MSCs of patients with AA, means ± SEM, $^*P < 0.05$). (**E**) Experimental design. Subgroups of patients with AA whose BM produced expandible MSCs (proliferated in culture) were collected (AA-MSCs). These AA-MSCs were compared with normal MSCs for expression levels of EMT factors and for HPC-supporting capacity. In another experiment, AA-MSCs were transfected with NC or anti-miR124-3p/miR-145-5p ASO and cocultured with $CD34^+$ cells to examine the effect of EMT activation in supporting capacity of AA-MSCs. (**F** to **H**) Restoration of HPC-supporting capacity of AA-MSCs by EMT activation. $CD34^+$ cells from normal donors were cocultured for 4 days with AA-MSCs transfected with scrambled ASO or ASO inhibiting miR-124-3p and miR-145-5p (EMT-activating ASO). Shown are the numbers of $CD45^+$ (F), $CD45^+CD34^+$ (G), and $CD45^+CD34^+CD90^+$ cells (H) and summary of the HPC expansion folds in EMT-activated MSCs relative to NC-MSCs in normal donor or AA-MSCs (**I**) ($n = 8$ from four MSCs of patients with AA, means ± SEM, $^*P < 0.05$).

results demonstrate that EMT-activated MSCs support NPCs and enhance neuronal tissue regeneration after neurotoxic injury, suggesting their potential application for neuronal regeneration.

aEMT-MSCs promote cardiac regeneration following myocardial infarction

Based on our findings on the regenerative potential of aEMT-MSCs in nonhematopoietic tissue, we also sought to explore their effects in the cardiovascular system. We began by examining their effects on two key cellular components of cardiac regeneration: ECs and cardiomyocytes.

Coculture of ECs with aEMT-MSCs enhanced proliferation, migration, and capillary formation with increased mesh formation in Matrigel assays compared to control MSCs, indicating enhanced angiogenic effects of ECs (Fig. 7, A to C). Moreover, aEMT-MSCs promoted the proliferation of c-Kit^+ cardiac progenitor cells (CPCs), as evidenced by a significantly higher proportion of human fetal cardiac progenitor cells (hCPCs) with reduced Hoechst 33342 intensity

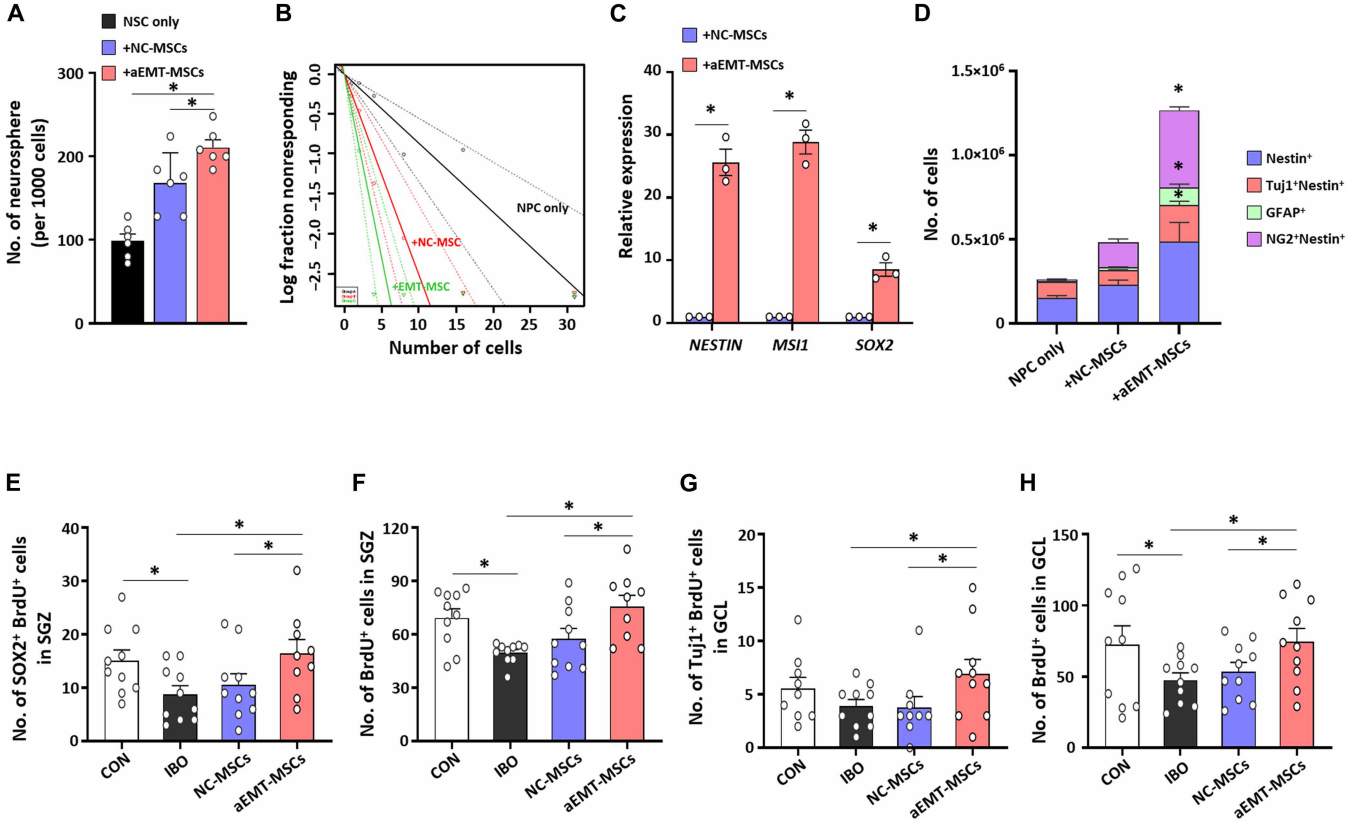

Fig. 6. Enhancement of neuronal regeneration by EMT-activated MSCs. (**A**) Sphere-forming assay performed on sorted NPCs after 3 days coculture with NC-MSCs or aEMT-MSCs. Numbers of neurosphere in each well plated with 1000 neuronal cells are shown ($n = 6$, means ± SEM, $*P < 0.05$). (**B**) Limiting dilution analysis for neurosphere formation during 3 days coculture of NPCs with NC-MSCs or aEMT-MSCs ($n = 8$, means ± SEM, $*P < 0.05$). (**C**) Relative expression of NPC-related genes in NPCs after 3 days coculture with NC-MSCs or aEMT-MSCs ($n = 3$, means ± SEM, $*P < 0.05$). (**D**) Lineage analysis of NPCs after 4 days coculture with NC-MSCs or aEMT-MSCs ($n = 4$, two experiments, means ± SEM, $*P < 0.05$). (**E** to **H**) Effects of EMT-activated MSCs on in vivo neuronal regeneration analyzed in SGZ and GCL. IBO was injected into the entorhinal cortex for neuronal destruction in dentate gyrus granular cells and pyramidal cells, followed by injection of NC-MSCs or aEMT-MSCs into the hippocampus. Quantification of proliferating NPCs ($BrdU^+Sox2^+$) (E) and total $BrdU^+$ neuronal cells (F) in SGZ at 4 weeks after transplantation of NC-MSCs or aEMT-MSCs is shown ($n = 10$, means ± SEM, $*P < 0.05$). [(G) and (H)] Quantification of immature neuronal cells ($BrdU^+Tuj\text{-}1^+$) (G) and total $BrdU^+$ neuronal cells (H) in GCL at 4 weeks after transplantation of NC-MSCs or aEMT-MSCs is shown ($n = 10$, means ± SEM, $*P < 0.05$).

in aEMT-MSC cocultures (Fig. 7, D and E), suggesting the potential to facilitate regeneration in damaged cardiac tissues.

Based on these in vitro results, the therapeutic potential of aEMT-MSCs was assessed in a myocardial infarction model induced by ischemia-reperfusion via ligation of the left anterior descending coronary artery for 60 min and subsequent reperfusion. aEMT-MSC transplantation into the peri-infarct zone significantly reduced necrosis compared to controls, with comparable areas at risk (Fig. 8, A to C). These protective effects persisted for at least 14 days, with aEMT-MSC–treated myocardium exhibiting a higher percentage of viable tissue in the infarct area than control MSC-treated myocardium (Fig. 8, D and E).

Histological analysis was performed on the transplanted hearts 4 weeks post-myocardial infarction (MI) to further investigate the repair of damaged heart tissue. Masson's trichrome (MT) staining revealed significantly reduced fibrosis and increased viable myocardium in the left ventricle (LV) wall of the aEMT-MSC group compared to controls (Fig. 8, F to H), indicating more efficient suppression of cardiac remodeling. Furthermore, the aEMT-MSC–treated hearts exhibited a significantly higher capillary density in the infarct and border zones, as determined by isolectin $B4^+$ ($IsB4^+$) cell quantification (Fig. 8, I to K), suggesting an enhanced vascularization in the damaged heart tissue. These histological results suggest that aEMT-MSCs enhance the regenerative microenvironment through both antifibrotic and angiogenic mechanisms. In addition, tracking of transplanted aEMT-MSCs revealed increased numbers of MSC-derived capillaries ($IsB4^+DiI^+$ ECs) and myocardial cells ($cTnT^+/DiI^+$ or $Cx43^+/DiI^+$) integrated into cardiac tissue (figs. S13 and S14), indicating an enhanced cardiovascular differentiation potential compared to control MSCs.

To evaluate the therapeutic effects of aEMT-MSCs on cardiac function, we performed both noninvasive and invasive assessments. The noninvasive serial echocardiography demonstrated significantly improved cardiac function in the aEMT-MSC group compared to control groups, as evidenced by higher left ventricular ejection fraction (LVEF) and fractional shortening (FS) percentages (Fig. 9, A to C). To further analyze the hemodynamics in the transplanted heart, we conducted invasive pressure-volume (PV) loop analysis at 4 weeks post-MI. This analysis revealed superior cardiac parameters in the aEMT-MSC group, including enhanced stroke volume (SV),

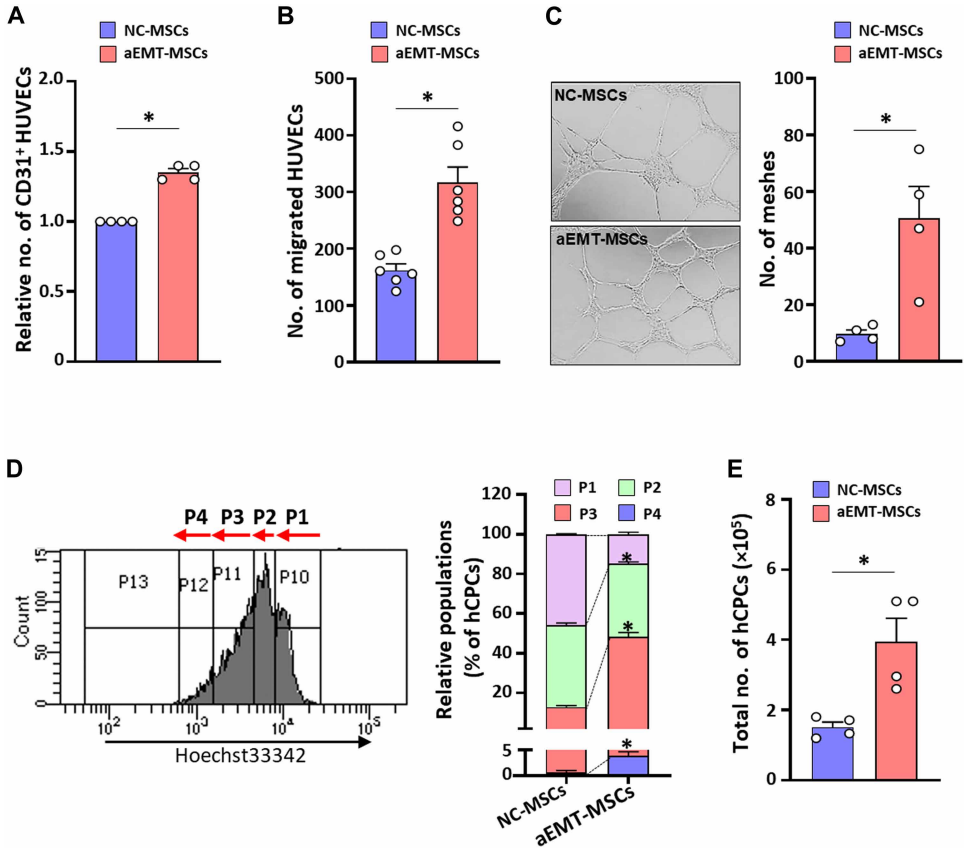

Fig. 7. Enhanced regeneration of cardiovascular cells by aEMT-MSCs. (**A** to **C**) Enhancement of capillary formation by aEMT-MSCs. (A) Effects on the expansion of ECs. Relative numbers of $CD31^+$ human umbilical cord endothelial cells (HUVECs) after coculture with NC-MSCs or aEMT-MSCs are shown ($n = 4$, two experiments, means ± SEM, $^*P < 0.05$). (B) Effects on the migration of ECs. HUVECs cocultured with NC-MSCs or aEMT-MSCs were compared for transwell migration toward serum. Shown are the numbers of HUVECs migrated through transwell after 24 hours ($n = 4$, two experiments, means ± SEM, $^*P < 0.05$). (C) Effects on tube formation. HUVECs cocultured for 2 days under each condition were plated on semisolid Matrigel. Shown are the representative images and numbers of meshes formed on Matrigel ($n = 4$, two experiments, means ± SEM, $^*P < 0.05$). (**D** and **E**) Effects on the proliferation of hCPCs. The hCPCs were labeled with Hoechst 33342 and cocultured with NC-MSCs or aEMT-MSCs for 4 days, then analyzed by flow cytometry for decrease of fluorescence intensity with mitotic division of hCPCs. Shown are the relative distribution of each mitotic populations (P1 ~ P4) (D) and total numbers of hCPCs after coculture (E) ($n = 4$, two experiments, means ± SEM, $^*P < 0.05$).

cardiac output (CO), and maximum (dp/dt_{max}) rates of pressure changes during contraction (Fig. 9, D to G). Similarly, load-independent contractility assessment via temporary inferior vena cava (IVC) occlusion provided further evidence of superior contractile function in the aEMT-MSC group, characterized by a steeper end-systolic pressure-volume relation (ESPVR), indicating enhanced intrinsic contractility, and a more gradual end-diastolic pressure-volume relation (EDPVR) slope, suggesting improved diastolic function (Fig. 9, H to J). These findings demonstrate that aEMT-MSC transplantation enhances both systolic and diastolic performance of the heart.

Notably, potential distinction in the damage mechanisms have been noted between the injury caused by ischemia and reperfusion, the latter being more related to oxidative stress (*51*). To see whether therapeutic effects of aEMT could be different between the two injury model, we also compared the effects on the myocardial infarction caused by permanent ligation (P/L) of the left coronary artery. We found comparable therapeutic effects on this P/L model in decrease of fibrosis, increase of viability, angiogenesis, and increase of LVEF as for injury caused by ischemic reperfusion (I/R) (fig. S15). Collectively, these findings suggest that aEMT-MSCs, endowed with enhanced EMT program and pericyte-like properties, demonstrate superior capacity for microenvironmental support and transdifferentiation potential, facilitating the regeneration of multiple tissue types (Fig. 10).

DISCUSSION

Microenvironmental regulation: The key to unlocking the potential of cell therapy

The microenvironment within stem cell niches plays a crucial role in regulating endogenous stem cell regeneration through a complex signaling cascade. This finely tuned process is mediated by the intricate cross-talk between stem cells and niche cells, highlighting the importance of targeting the microenvironment to enhance tissue regeneration (*5*, *52*, *53*).

The identification of MSCs as regenerative cells with paracrine effects has led to a substantial increase in clinical trials exploring MSC therapy to stimulate endogenous stem cell regeneration in a wide range of conditions, including hematopoietic, neuronal, and

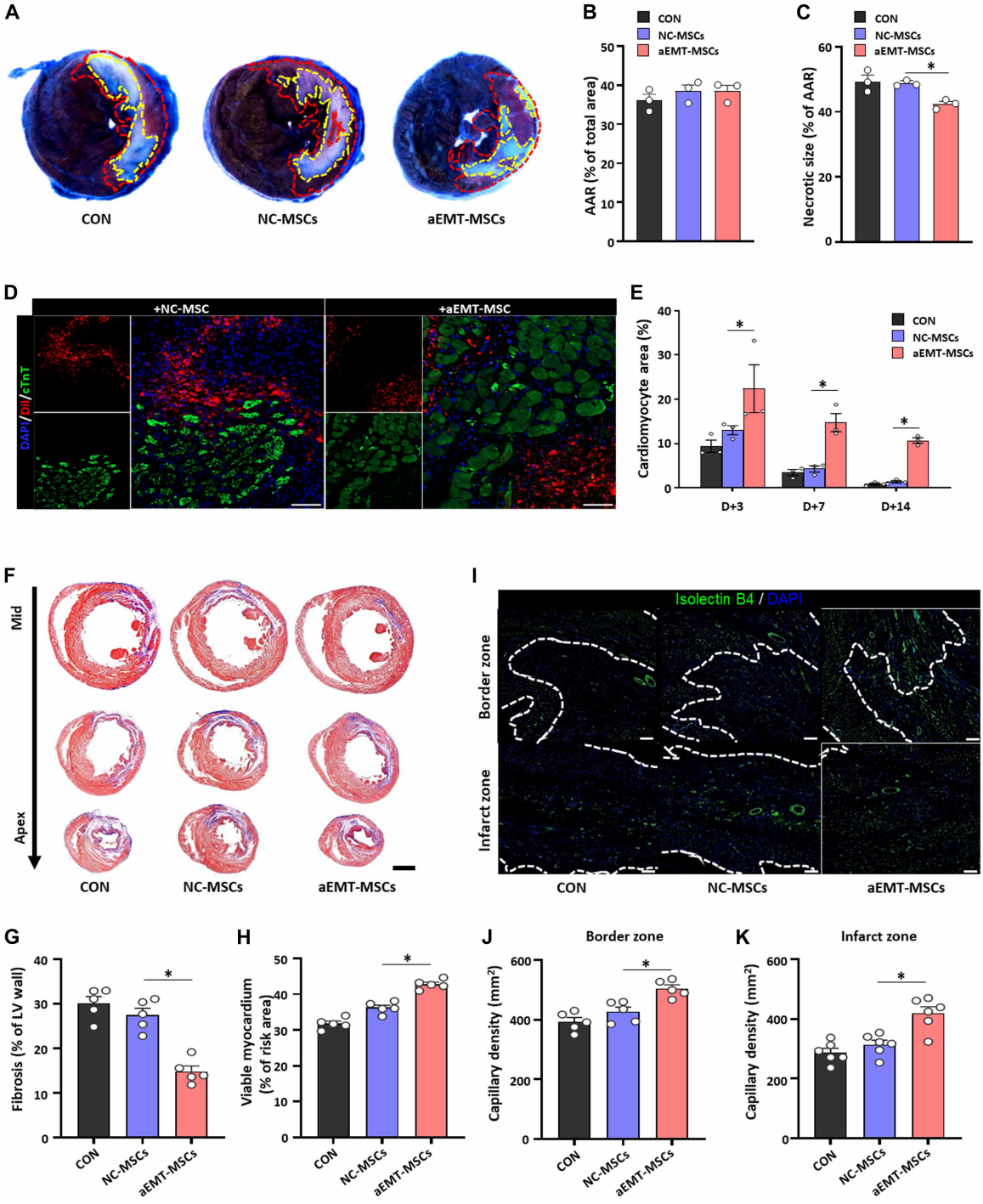

Fig. 8. Effects of aEMT-MSCs on the recovery of myocardium injured by I/R. Ischemic reperfusion injury (I/R injury) was induced by obstruction of the left anterior descending coronary artery for 60 min, followed by reperfusion and injection of NC or aEMT-MSCs in the peri-infarct region of the heart. (**A** to **E**) Protective effects of aEMT-MSCs. Infarct heart was examined 24 hours after transplantation and examined by triphenyltetrazolium chloride (TTC)/Evans Blue staining. Representative images (A), % area at risk (AAR) in total LV area (B), and % necrotic area in AAR (C) are shown ($n = 3$, means ± SEM, $^*P < 0.05$ compared to NC-MSCs group). (D and E) Survival of cardiomyocyte in the transplanted area. Infarct areas of the heart were transplanted with DiI-labeled NC or aEMT-MSCs and examined for viable myocardium (cTnT) (green) and DiI positive MSCs (red). Shown are the representative images for cTnT/DiI staining (D) and quantification of viable myocardium area at each indicated time point after myocardial infarction (E) ($n = 3$, means ± SEM, $^*P < 0.05$ compared to NC-MSCs group). D, day. (**F** to **H**) Effects of aEMT-MSCs on fibrosis of infarct heart. Representative images of MT staining in the heart tissues collected at 4 weeks after I/R injury (F). Scale bar, 2000 μm. % Area of fibrosis in LV wall (G) and % viable myocardium in AAR (H) are shown. (**I** to **K**) Effects on angiogenesis in the infarct area. Representative images of capillaries stained with fluorescein isothiocyanate (FITC)–IsB4 (green) on the border zone and infarct zone at 4 weeks after I/R injury (I). Quantification of capillary density in border (J) and infarct zone (K) ($n = 5$, means ± SEM, $^*P < 0.05$ compared to NC-MSCs group).

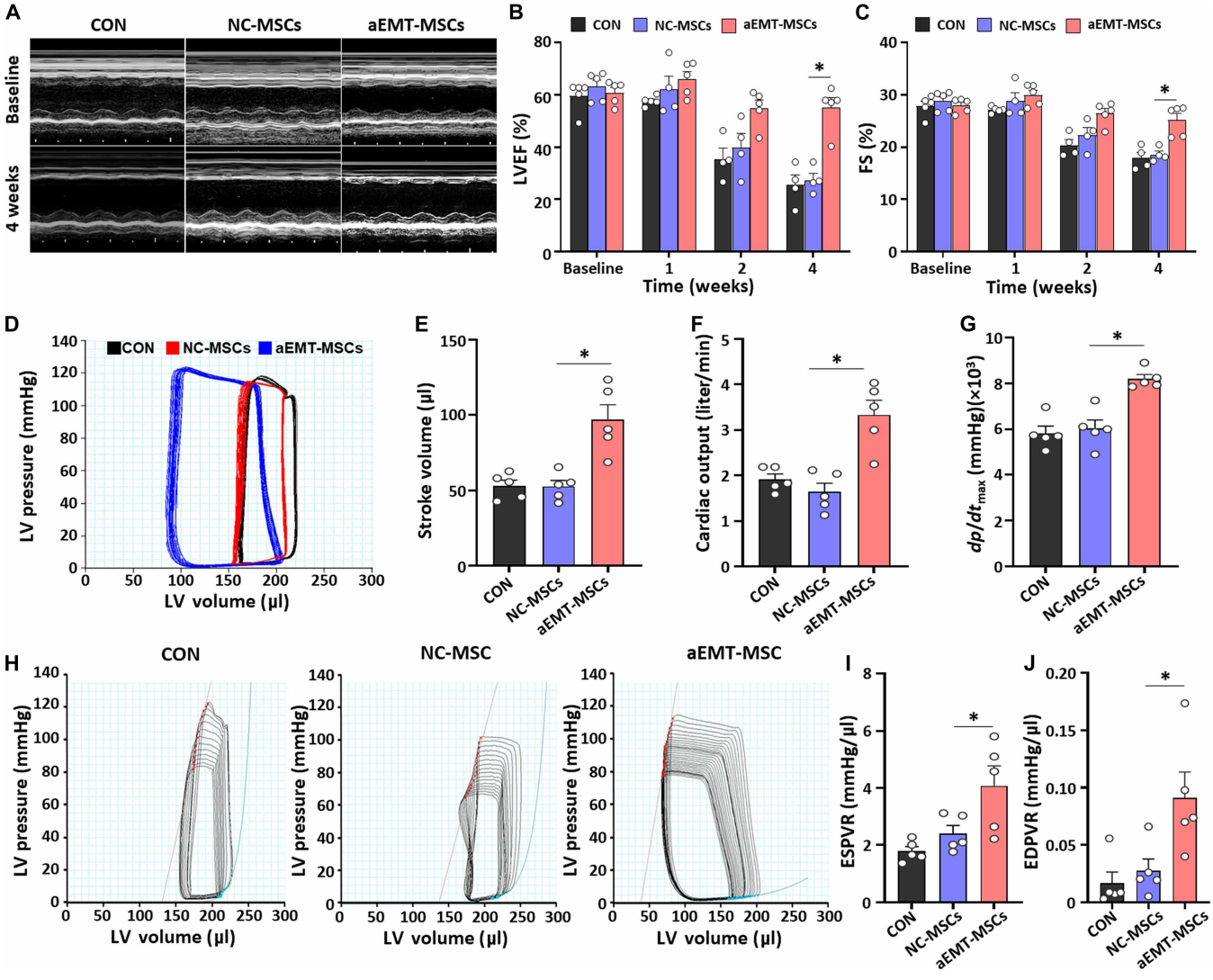

Fig. 9. Effects of aEMT-MSCs on inhibition of remodeling and recovery of cardiac function. (**A** to **C**) Evaluation of cardiac function by echocardiography. Representative M-mode images at 4 weeks posttransplantation (A). Comparisons for LVEF % (B) and FS % (C) in the heart transplanted with NC-MSCs or aEMT-MSCs are shown with group injected with buffer (CON) ($n = 5$, means ± SEM, $^*P < 0.05$). (**D** to **G**) Monitoring of hemodynamics by PV loops 4 weeks after transplantation. The representative image of the hemodynamic PV loops at 4 weeks (D). The quantitative value of each indicated hemodynamic measurement parameters for SV (E), CO (F), and kinetics of pressure loading during contraction assessed by *dp*/*dt* (G) were measured for comparison between each group ($n = 5$, means ± SEM, $^*P < 0.05$). (**H** to **J**) Monitoring dynamic changes of hemodynamics by transient occlusion of IVC. Representative images for PV loop for LV pressure with changes of LV volume induced by transient occlusion of IVC for each group are shown (H). Quantitative measurement of the slope of ESPVR (I) and EDPVR (J) during transient occlusion of IVC ($n = 5$, means ± SEM, $^*P < 0.05$).

cardiovascular disorders (*54*). Despite this potential, the suboptimal efficacy of MSC clinical trials has hindered their acceptance as standard-of-care interventions (*55*), and few MSC-based cell therapeutics have been accepted as standard-of-care interventions. To address this challenge, it is essential to decipher the mechanisms governing MSC niche activity and to develop strategies to modulate their regenerative capacity in cell therapy.

EMT gradient: A key regulator of microenvironmental support

In our study to elucidate the mechanisms that enhance niche activity, we focused on the association of the EMT in MSCs and regenerative effects based on several lines of evidence. First, it was demonstrated that the BM HSC niche-forming MSCs are distinctively developed from the neural crest through EMT, rather than from mesodermal origin (*23*). Second, a correlation was observed between higher EMT gradient and increased HSC-supporting activities in 3D spheroid MSCs (*22*). Furthermore, EMT progression in MSCs was frequently observed in various models of tissue regeneration (*56*–*58*). These findings collectively led us to hypothesize that the EMT gradient may function as a key regulator of MSC's supporting capacity.

We first examined this possibility in the hematopoietic system and investigated the functional significance of the EMT gradient in

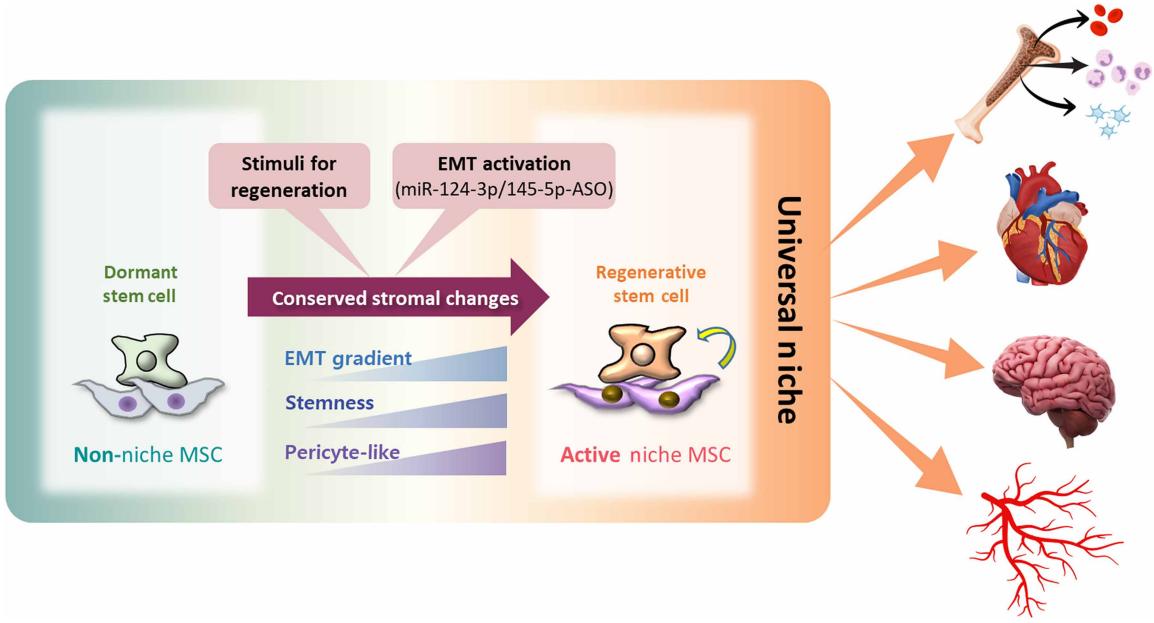

Fig. 10. Schematic illustration of conserved stromal changes underlying the activation of niche function. MSCs lacking niche function fail to support stem cell self-renewal or regeneration. Upon physiological stimuli for regeneration, MSCs undergo stromal changes characterized by a triad: increased EMT gradient, induction of stemness-associated genes, and acquisition of pericyte-like features. These stromal changes can be reproduced by inhibiting miRNA-124-3p/145-5p in MSCs, which enhances the EMT gradient and stemness gene expression, thereby recapitulating the activated mesenchymal niche. These conserved stromal changes in MSCs serve as broad-spectrum, universal niche cells that can support regeneration across multiple tissues, including hematopoietic, neuronal, and cardiovascular systems.

MSCs. Our findings revealed that the mesenchymal niche within the BM exhibits a hierarchical organization with respect to the EMT gradient under in vivo conditions. Moreover, we observed that the dynamic control of niche activities by biological stimuli was accompanied by concomitant changes in the EMT gradient, a phenomenon also observed under pathological conditions, such as leukemia or AA. These observations demonstrated that the EMT gradient in MSCs serves as a key parameter for regulating the microenvironmental support of stem cells under both physiological and pathological conditions of the BM.

While the complete mechanisms linking the EMT gradient to enhanced niche activity remain under investigation, 3D-MSCs with a higher EMT gradient exhibited higher expression of growth factors supporting HSCs (*22*). In accordance with this observation, MSCs engineered for a higher EMT gradient through miR-124-3p/miR-145-5p inhibition demonstrated similar molecular profiles characterized by enhanced expression of genes associated with cell-cell interaction and activation of signaling pathways that mediate regenerative processes. These findings suggest that the changes in EMT gradient should be accompanied by a transcriptional reprogramming that involves comprehensive changes priming the cells for higher niche activity.

Stemness and pericyte phenotype: Hallmarks of EMT-activated MSCs

The increase in EMT gradient during niche activation was accompanied by the acquisition of a molecular signature mimicking stem cells expressing pluripotency genes, suggesting a link between the stem cell–like state and niche function. Further evidence supporting this connection comes from 3D cultured MSCs with higher EMT gradient, which displayed increased epigenetic plasticity and dynamic chromatin transitions, recapitulating stem cell epigenetic characteristics (*22*, *59*, *60*). In addition, the acquisition of a stem cell–like phenotype in the mesenchymal niche was observed during adaptive BM niche activation induced by 5-FU treatment (*16*).

Notably, the functional link between EMT and stemness is a recurring theme in various biological contexts beyond the BM hematopoietic system. For example, EMT induction in normal breast epithelial cells is associated with acquiring stem cell properties (*61*). Furthermore, EMT is often linked to stemness in cancer cells, with cancer stem cells exhibiting enhanced EMT (*62*). In this light, it is plausible that an elevated EMT gradient likely indicates a state of cellular plasticity that facilitates the acquisition of stem-like properties, thereby priming cells for regenerative microenvironment. However, it is noteworthy that potential heterogeneity also exists in EMT programs in its extent and in molecular changes associated EMT progression, as distinct spectrums of EMT signatures are observed in different context of cell fate transition (*63*, *64*), necessitating further investigation to elucidate the precise nature of EMT process during the control of niche activity.

On the other hand, EMT induction is associated with the conversion of MSCs into pericyte-like cells. Pericytes in vascular niches play a pivotal role in supporting regeneration across multiple tissues (*30*, *47*, *65*). The transition of stromal cells into pericyte-like cells often correlates with enhanced niche activity; for example, in lung injury models, pericyte-like cells increase in the lesion and show transcriptional changes toward regenerative processes (*66*). In addition, MSCs derived from induced pluripotent stem cells of the same donor, with enhanced supportive function, display higher pericyte marker induction (*67*). These observations support the hypothesis that niche activation is characterized by a triad of EMT-activating

programs, including EMT activation, pluripotency gene induction, and pericyte phenotype acquisition (Fig. 10).

Engineering MSCs for enhanced stem cell support and disease therapy

Providing direct support for the hypothesis that the EMT gradient reflects the status of niche activation, we engineered MSCs with miRNA inhibitors to induce EMT gradient elevation. Notably, these engineered aEMT-MSCs exhibited activation of niche function accompanied by EMT elevation, stemness acquisition, and pericyte-like changes, replicating the niche activation program with the triad EMT program observed in "stimulated" MSCs. Moreover, while thus engineered aEMT-MSCs demonstrated a significant enhancement of normal HSC regeneration with long-term repopulation, this approach also proved effective in ameliorating the defective niche function of MSCs derived from patients with AA. Moreover, enhancing the EMT gradient in MSCs from patients with AA restored the clonogenic potential of AA-MSCs, while hematopoietic cells from these patients retained their capacity for expansion in response to stimulation by aEMT-MSCs. Collectively, these findings suggest the feasibility of reversing key pathological features of AA, despite the limited cell numbers typically observed under this condition.

However, considering the multi-etiological origin of AA, including cell-autonomous defects of HSCs in addition to microenvironmental origin (*68*), further investigations are necessary to evaluate the therapeutic potential of EMT-activated MSCs in ameliorating the hematological insufficiency in AA BM.

Although aEMT-MSCs supported normal hematopoietic cells, including those derived from patients with AA, they did not support the expansion of leukemic cells tested (fig. S7, A to D). Similarly, hematopoietic cells expanded in the presence of aEMT-MSCs did not display clonal dominance or lineage bias during BM reconstitution (fig. S7, E and F), indicating preservation of normal BM repopulation. Moreover, given that aEMT-MSCs are generated through RNA-based ASO targeting of miRNAs, these findings collectively underscore the safety of this strategy for translational application.

Extending the scope of EMT-activated MSCs across multiple tissue type

The association of EMT with regeneration processes in various tissue types provides a compelling rationale for extending the application of EMT-activated MSCs beyond the hematopoietic system. EMT has been implicated in the generation of renal progenitors and the repair of the gastrointestinal tract, corneal epithelium, and other tissues (*57*, *69*–*71*), suggesting that EMT may serve as an intrinsic adaptive response of stromal cells to tissue injury, thereby facilitating regeneration across a wide range of tissues. In line with this notion, we observed efficient support of aEMT-MSCs on NPCs and enhanced regeneration of neuronal tissues in the hippocampus in response to damage induced by neurotoxic drugs.

Similarly, aEMT-MSCs demonstrated stimulatory effects on cells of the cardiovascular system, which were demonstrated upon transplantation into the ischemia-reperfusion-damaged myocardium. Notably, EMT-activated MSCs conferred enhanced myocardial protection, reduced infarct area, increased angiogenesis, and ultimately led to greater recovery of cardiac function compared to control MSCs, which was comparable for both I/R and P/L model.

EMT-activated MSCs also generated significantly higher numbers of MSCs taking the phenotypes of ECs and cardiomyocytes in the infarct region. In accordance with previous observation for transdifferentiation potential of MSCs into ECs or smooth muscle cells (*72*, *73*), these findings raise the intriguing possibility that EMT-activated MSCs may have a higher potential for transdifferentiation, possibly due to their acquisition of stemness and increased plasticity. Accordingly, it is possible that aEMT might contribute to regeneration of vessel or cardiomyocytes in addition to their supportive function on CPCs. However, further studies are required to validate the functional contribution of these MSC-derived cells for regeneration of myocardium. Nevertheless, our study demonstrated the potential of modulating the EMT gradient as a strategy for microenvironmental activation and regeneration across multiple tissue types.

Harnessing the power of EMT for regenerative medicine

In conclusion, our investigations identified the EMT program as a crucial parameter and determinant of microenvironmental niche activities that can enhance regenerative processes in multiple tissue types. This research opens avenues for developing innovative niche-targeting strategies, paving the way for advances in the field of regenerative medicine.

MATERIALS AND METHODS

Human samples and culture

BM from patients with AML and patients with AA was obtained with Institutional Review Board (IRB) approval (KC15TISI0973 and KC17TESI0426) and listed in table S1. Human BM MSCs derived from healthy donors were obtained with informed consent, following approval by the IRB of The Catholic University of Korea (MC-19SNSI0059). Umbilical cord blood (UCB) was obtained directly from healthy pregnant women donors under written informed consent (CUMC11U077). This study was approved by the IRBs of St. Mary's Hospital and The Catholic University of Korea. BM MSCs from patients with AML, patients with AA, and healthy donors were cultured in low-glucose Dulbecco's modified Eagle's medium (Hyclone Laboratories Inc., Schenectady, NY, USA) supplemented with 15% fetal bovine serum (FBS; Hyclone), penicillin (100 U/ml), streptomycin (100 mg/ml), and L-glutamine (Gibco, Grand Island, NY, USA) in a humidified atmosphere of 5% CO_2 at 37°C.

Colony formation and osteogenic and adipogenic differentiation of MSCs

For colony formation (CFU-F), MSCs were plated at a density of 1000 cells per 100-mm dish, and after incubation for 14 days, the number of colonies containing >50 cells was counted after staining with crystal violet (Sigma-Aldrich, Carlsbad, CA, USA). Osteogenic and adipogenic differentiation of MSCs was performed as previously described (*67*), followed by Alizarin Red S (Sigma-Aldrich) or Oil Red O (Sigma-Aldrich) staining, respectively. The osteogenic mineralization or adipogenic lipid droplets were eluted and quantitatively measured by spectrophotometry at 450 and 510 nm, respectively.

Analysis using the public RNA-seq database and dbEMT

Transcriptomic analysis was performed using publicly available RNA-seq datasets (GSE61695) (*23*) to compare gene expression profiles

between NESTIN$^+$PDGFRα$^+$ and NESTIN$^-$PDGFRα$^-$ MSCs. To specifically assess the expression of EMT-related genes, curated gene sets from the dbEMT (*24*) database were used.

Ex vivo culture of CD34$^+$ cells from normal hematopoietic or leukemia cells

Normal human CD34$^+$ cells from UCB or leukemic CD34$^+$ cells from BM were isolated by an immunomagnetic column using Dynabeads (Invitrogen, Carlsbad, CA, USA) according to the manufacturer's instructions. MSCs were irradiated with 1500 cGy 24 hours before coculture with normal or leukemic CD34$^+$ cells for 4 days in culture medium in the presence of a cytokine mixture [human stem cell factor (100 ng/ml), human Flt3-Ligand (100 ng/ml), and human interleukin-3 (IL-3), IL-6, and G-CSF (20 ng/ml); ProSpec-Tany TechnoGene Ltd.]. For the colony-forming assay of hematopoietic progenitors, hematopoietic cells were plated for 14 days in semisolid methylcellulose medium (MethoCult; STEMCELL Technologies, Vancouver, BC, Canada) containing cytokines and analyzed for colony numbers and lineages as described (*67*).

Flow cytometry

Cocultured cells were analyzed by flow cytometry (LSR II) using the following antibodies: hCD45-APC (1:50), hCD34-PE (1:25), and hCD90-FITC (1:100) (BD Pharmingen, USA). Hematopoietic stem progenitor cells (HSPCs) in recipient mouse BM cells were analyzed using the following antibodies: hCD45-APC (1:50), hCD34-PE (1:25), and hCD38-PE-cy7 (1:20) (BD Pharmingen). Cells were stained for 30 min on ice after adding the optimal concentration of antibody.

MSC activation using PIPC and sub-P

MSCs were incubated with or without 50 μg/ml of PIPC (Sigma-Aldrich) or 10 nM of sub-P (Sigma-Aldrich) for 3 days for sample collection for RNA preparation. CD34$^+$ cells from UCB were cocultured for 4 days with control MSCs or stimulated MSCs.

Delivery of target miRNAs or siRNA into MSCs

The miR-145-5p inhibitor and miR-124-3p inhibitor were purchased from Bioneer (Daejeon, Korea). Human mesenchymal stromal cells (MSCs) were cultured in Opti-MEM (Gibco) and transfected with 30 nM miR-145-5p inhibitor and 30 nM miR-124-3p inhibitor using oligofectamine (Invitrogen). Scrambled miRNA was used as an NC.

MSCs were transfected with a mixed siRNA at 20 nM each targeting EMT-related genes (*SNAI1*, *SLUG*, *ZEB1*, and *TWIST1*) (Bioneer) using oligofectamine. Scrambled siRNA was used as an NC.

NSG mice repopulation assay

NSG mice were irradiated with 250 cGy and intravenously injected with hematopoietic cells cocultured on MSCs. Human cell engraftment was analyzed as described previously (*60*). To evaluate the level of human HSPC engraftment, cells were collected by femoral BM aspiration at 6 weeks posttransplant and stained with hCD45-APC, hCD34-PE, and hCD38-PE-cy7 antibodies according to the manufacturer's instructions.

CRU assay

For secondary transplantation, BM cells harvested from primary recipients were pooled and transplanted into secondary NSG mice that had been conditioned with sublethal irradiation (250 cGy) 24 hours before injection. The BM cells from primary recipients were diluted to the indicated cell number and injected into each secondary mouse. At 14 weeks post–secondary transplantation, BM cells were harvested, and engraftment and population of HSPCs were assessed by flow cytometry using human-specific antibodies against CD45, CD34, and CD38 (BD). One CRU was defined as the cell dose resulting in 37% of the mice tested being negative (*46*). CRU frequencies and 95% confidence intervals were calculated by applying Poisson statistics to the proportion of negative mice from groups of recipients transplanted with different numbers of cells using the L-Calc software (STEMCELL Technologies).

Real-time polymerase chain reaction

Total RNA was extracted from MSCs using TRIzol (Invitrogen). cDNA was synthesized with reverse transcriptase (Invitrogen) for mRNA or the miScript II RT Kit (QIAGEN, Hilden, Germany) for miRNA. Real-time quantitative polymerase chain reaction (RQ-PCR) was performed with the QuantStudio 3 Real-Time PCR System (Applied Biosystems) and SYBR Premix Ex Taq (Takara, Japan). Relative levels of PCR products were determined after normalizing to an endogenous 18*S* ribosomal RNA (rRNA) for mRNA or U6 for miRNA control. The relative mRNA expression was calculated using the formula $2^{-\Delta\Delta Ct}$, where $\Delta Ct = Ct_{sample} - Ct_{reference}$ and $\Delta\Delta Ct = \Delta Ct_{sample} - \Delta Ct_{control\ group}$.

Neurosphere formation and limiting dilution assay

For the neurosphere formation assay, NPCs were sorted after 3 days of coculture with NC-MSCs or EMT-MSCs and plated at 1000 cells. Cell counting was performed 4 days after plating. For the limiting dilution assay, NPCs were plated at limiting dilution doses on a low attachment 96-well plate (Corning, NY, USA) with B27 medium for 4 days.

IBO-induced brain injury model

Male Sprague-Dawley rats (220 to 250 g) were purchased from Orient Co. (Seoul, Korea). Rats were housed two or three per cage, allowed access to water and food ad libitum, and maintained under constant temperature (23° ± 1°C), humidity (60 ± 10%), and a 12-hour light/dark cycle (light on 0700 to 1900). Animal maintenance and treatment were carried out in accordance with the Animal Care and Use Guidelines issued by Kyung Hee University, Korea. All experiments with rats were performed according to the protocols approved by the Institutional Animal Care and Use Committee (IACUC) of Kyung Hee University [approved protocol number KHUASP(SE)-13-031].

Stereotaxic injection of IBO was performed as previously described (*49*). Rats were anesthetized with equithensin [350 mM sodium pentobarbital, 250 mM chloral hydrate, 85 mM $MgSO_4$, and 40% propylene glycol in 10% ethanol (2 ml/kg)]. IBO (3 μl per animal, 1 mg/ml in 0.9% saline) or an equal amount of saline (for the Sham group) was injected into the entorhinal cortex as follows: Rats were placed in a stereotaxic device (Stoelting) with the incisor bar 3.4 mm below the interaural line, and the needle was positioned at an angle of 10° right to the midsagittal plane. IBO or saline was injected at three different locations on both sides of the entorhinal cortex of the cerebral hemispheres. For the IBO + NC-MSC or aEMT-MSC groups, IBO-injected rats received bilateral infusions of NC-MSCs or aEMT-MSCs into the dentate gyrus (hilus) of the hippocampus. Two microliters of NC-MSCs or aEMT-MSCs (3 ×

10^4 cells/μl) was injected into the site. For the nonimplanted groups (IBO group and Sham group), rats received an equal amount of vehicle without cells (saline) in the dentate gyrus. The syringe was left at the injected position for 10 min and then withdrawn over 5 min to minimize loss of cells from the injection site.

Immunohistochemistry for brain tissue

Animals were sacrificed and perfused with 4% paraformaldehyde in phosphate-buffered saline (PBS). Following immersion fixation with 4% paraformaldehyde in PBS for 4 hours, the brains were cryoprotected in 30% sucrose-PBS and then frozen with optimal cutting temperature (OCT) compound and stored at −80°C until processed. Brain tissue blocks were cryosectioned through the coronal plane at a thickness of 35 μm. Sections were stored at 4°C in storing solution (30% glycerol and 30% ethylene glycol in PBS). The cryosectioned brain slices (35 μm) were permeabilized in 0.5% Triton X-100 for 20 min and blocked in 15% normal serum with 3% bovine serum albumin and 0.1% Triton X-100 for 2 hours while free-floating. The sections were incubated overnight at 4°C with primary antibodies: anti-BrdU (Abcam, ab6326), anti-Tuj1 (Sigma-Aldrich, t8660), anti-NeuN (Merck, mab377b), and anti-Sox2 (R&D Systems, mab2018), followed by incubation with Alexa Fluor 488– or Cy3-conjugated secondary antibodies. For quantification, images were captured by an LSM 800 confocal microscope (Carl Zeiss, Germany) and analyzed using ImageJ software [National Institutes of Health (NIH)].

Capillary formation and migration assay of human umbilical cord endothelial cells

For the capillary tube formation assay, cell culture plates were coated with Matrigel (Corning) and incubated for 1 hour at 37°C to promote gelation. Human umbilical cord endothelial cells (HUVECs) cocultured with NC-MSCs or aEMT-MSCs were plated on the Matrigel for 16 to 18 hours at 37°C. Capillary tubes were observed with a microscope, and images were quantified using ImageJ software. For the migration assay, HUVECs were cocultured with MSCs for 3 days, and sort-purified HUVECs were added to a transwell insert (8-μm pore size) and allowed to migrate toward serum. After 24 hours of incubation, HUVECs that migrated to the underside of the transwell insert were fixed and stained with crystal violet.

Culture of human c-Kit$^+$ CPCs and proliferation assay

Human c-Kit$^+$ cells were cultured in Ham's F-12 medium (Hyclone) containing 10% FBS (Gibco), 1% penicillin-streptomycin (Gibco), 5 μg of recombinant human basic fibroblast growth factor (PeproTech, Rocky Hill, NJ, USA), 2.5 U of human erythropoietin (R&D Systems, Minneapolis, MN, USA), and 2 mM glutathione (Sigma-Aldrich). To determine the division of cell populations undergoing proliferation, Hoechst 33342 staining (Invitrogen) was used. The division of cells was analyzed by flow cytometry (LSR II).

Myocardial infarction and cell injection

All animal studies were approved by the IACUC of The Catholic University of Korea (approval number CUMC-2021-0037-04). All animal procedures conformed to the NIH guidelines or the guidelines issued by Directive 2010/63/EU of the European Parliament for the protection of animals used in scientific research. Fisher 344 rats (160 to 180 g, 8-week-old males; Central Lab Animal Inc., Korea) were anesthetized with 2% inhaled isoflurane and intubated with an 18-gauge intravenous catheter in the trachea. The rats were ventilated with a rodent respirator (Harvard Apparatus). A 37°C heating pad was used to maintain their body temperature throughout the operation. The chest was shaved and sterilized with 70% alcohol. Ischemia-reperfusion injury was induced by occluding the left anterior descending (LAD) artery with a 7-0 Prolene suture for 60 min. A total of 1×10^6 NC-MSCs or aEMT-MSCs suspended in 50 μl of PBS were injected into the border zone of the infarcted myocardium at two sites (25 μl each), 5 min prior to reperfusion following LAD occlusion. In the P/L model, the LAD artery was permanently ligated using the same 7-0 Prolene suture, and cells were injected immediately after ligation using the same injection protocol. To trace the injected cells within the heart tissues further, MSCs were prelabeled with a red fluorescence dye, CellTracker CM-DiI (Invitrogen), prior to cell injection. NC-MSCs and aEMT-MSCs were incubated in the CM-DiI Dye solution (5 μg/ml) for 5 min at 37°C, followed by additional 15 min at 4°C. After labeling, BM MSCs were washed with PBS and resuspended in serum-free medium for further uses. Then, the chest was closed aseptically, cleansed with 0.9% normal saline solution, and treated with topical antibiotics.

Measurement of myocardial infarct size

Combined Evans Blue and triphenyltetrazolium chloride (TTC) staining was performed to determine the early cardioprotective effects of aEMT-MSCs. Rats were anesthetized and ventilated as described previously. After 60 min of ischemia and 24 hours of reperfusion, the suture thread around the LAD artery was retied, and Evans Blue dye (8% in PBS) was injected intravenously into the rats. After 20 min, the heart was quickly excised and incubated for 25 min at −4°C. The heart was cut into three slices (each one ~2-mm thick) and incubated with 2% TTC for 30 min at 37°C in the dark. After being washed with PBS three times, the tissue was fixed in 4% paraformaldehyde. The noninfarcted myocardium was stained deep blue with Evans Blue. The viable myocardium was stained red with TTC. The necrotic myocardium appeared white after TTC staining. The area at risk (AAR) and the necrotic area were determined digitally using ImageJ.

Echocardiography

The assessment of functional improvement in injured cardiac tissues was performed with echocardiography. Rats were lightly anesthetized with inhaled isoflurane, and physiological data were recorded using a transthoracic echocardiography system equipped with a 15-MHz L15-7io linear transducer (Affiniti 50G, Philips). Serial echocardiograms were performed at 6 hours after I/R modeling (baseline) and 1, 2, and 4 weeks after treatment. In the P/L model, echocardiographic assessment was conducted at 1, 2, 4, and 8 weeks after cell transplantation. The echocardiography operator was blinded to the group allocation during the experiment. Ejection fraction (EF) and FS, which are indexes of LV systolic function, were calculated with the following equations, respectively

$$\text{EF}\ (\%) = [(\text{LVEFDD}^3 - \text{LVESD}^3)/\text{LVEDD}^3] \times 100$$
$$\text{FS}\ (\%) = [(\text{LVEDD} - \text{LVESD})/\text{LVEDD}] \times 100$$

Hemodynamic measurements

Hemodynamic measurements were performed at the 4-week endpoint, prior to euthanasia. Rats were anesthetized and ventilated as

described previously. After thoracotomy, the LV apex of the heart was punctured with a 26-gauge needle, and a 2F conductance catheter (SPR-838, Millar) was inserted into the LV. LV PV parameters were continually recorded using a PV conductance system (MPVS Ultra, emka TECHNOLOGIES, Paris, France) coupled to a digital converter (PowerLab 16/35, ADInstruments, Colorado Springs, CO, USA). Load-independent parameters of cardiac function, including the slopes of the ESPVR and EDPVR, were measured at different preloads, which were elicited by transient occlusion of the IVC with a needle holder. Fifty microliters of hypertonic saline (20% NaCl) was injected into the left jugular vein to calculate the parallel conductance after hemodynamic measurements. Blood was collected from the LV into a heparinized syringe and transferred into cuvettes to convert the conductance signal to volume using the catheter. The absolute volume of the rat was defined by calibrating the parallel conductance and the cuvette conductance.

Capillary density measurement

Five heart sections with 4-μm thickness were preincubated in a 37°C dry oven before deparaffinization and rehydration. The sections were blocked and incubated with primary antibody at 4°C overnight. The sections were washed three times with PBS and incubated for 1 hour with secondary antibodies at room temperature. The samples were then washed, mounted with a mounting medium, and photographed using a fluorescence microscope (Nikon, Tokyo, Japan). The number of blood vessels was counted in five random microscopic fields per sample.

Determination of fibrosis area

MT staining (Sigma-Aldrich) was performed to determine the fibrosis area of MI hearts. Briefly, three frozen sections were fixed in Bouin's solution at 56°C for 90 min in each group. These sections were stained using Weigert's Iron Hematoxylin Solution for 5 min at room temperature and also stained using Biebrich Scarlet-Acid Fuchsin Solution for 25 min at room temperature. Last, the sections were counterstained with Aniline Blue for 25 min, followed by incubation in 1% acetic acid for 2 min at room temperature. The collagen fibers appeared blue, and viable myocardium appeared red. The percent of the area of fibrosis to the entire LV wall area was quantified using ImageJ software with basic add-ons.

Immunohistochemistry for heart tissue

The hearts were excised at 28 days following NC-MSCs and aEMT-MSC transplantation and fixed with 4% paraformaldehyde. The tissues were then embedded in a paraffin block and sectioned into 4-μm slices. The sections were deparaffinized, and antigen retrieval was performed using a retrieval solution (DAKO, K8005). Subsequently, the sections were permeabilized in PBS containing 0.5% Triton X-100 for 15 min and then probed at 4°C with primary antibodies diluted in an antibody diluent containing background reducing components (DAKO, S3022). Primary antibodies used in this study include mouse anti-TNNT2 (Abcam; 1:200), rabbit anti-CD31 (Abcam; 1:200), and rabbit anti-GJA1(CX43) (Abcam; 1:50). After washing three times with 1% Tween 20 in PBS, the samples were incubated with secondary antibodies for 60 min at room temperature in the dark. Secondary antibodies used in this study include either anti-mouse immunoglobulin G (IgG) Alexa Fluor 488 (Invitrogen; 1:500), anti-mouse IgG Alexa Fluor 647 (Invitrogen; 1:250), and anti-rabbit IgG Alexa Fluor 488 (Invitrogen; 1:500). After washing again with PBS, the sections were stained with 4′,6-diamidino-2-phenylindole (DAPI) solution (VectaShield) for nuclear staining and then mounted on slides. Images of the heart sections were visualized using an LSM 800 laser scanning microscope with Airyscan processing (Zeiss).

Liquid chromatography and tandem mass spectrometry

The cells were disrupted in a lysis buffer containing 2% SDS, 2 mM $MgCl_2$, 50 mM triethylammonium bicarbonate, and 1× Halt phosphatase and protease inhibitors (Thermo Fisher Scientific, Waltham, MA, USA), followed by sonication using a Bioruptor Sonicator (Diagenode, Denville, NJ, USA). Proteins were recovered and proteolyzed with trypsin on S-trap columns (ProtiFi, Fairport, NY, USA). The resultant peptide samples were reconstituted in 0.1% acetic acid, and an aliquot containing 1 μg/μl of the sample was injected into an EASY-Spray column (75 μm internal diameter by 500 mm, 2 μm, 100 Å; Thermo Fisher Scientific) on an UltiMate 3000 RSLC nanochromatography system at a flow rate of 300 nl/min. The LC system was connected to a Q-Exactive mass spectrometer (Thermo Fisher Scientific) operating in data-dependent acquisition mode. Survey full-scan MS spectra (300 to 1600 mass/charge ratio) were acquired with a resolution of 70,000.

Analysis of MS data (peptide and protein identification and quantification)

The MS data were processed using the Proteome Discoverer (v2.2.0.388) software. Protein identification was performed against the human UniProtKB database (released in June 2020). Search parameters were 10 parts per million for precursor mass tolerance, 0.02 Da for fragment mass tolerance, two missed trypsin cleavage sites, cysteine carbamidomethylation (+57.021 Da) as a fixed modification, methionine oxidation (+15.9949 Da), and N-terminal protein acetylation (+42.0106 Da) as variable modifications. The false discovery rate was set to 0.01 for proteins and peptides and was determined by searching a reverse database. The minimum number of razor and unique peptides in a protein group was considered as two peptides for protein identification.

Peptide abundance was quantified using the Minora Feature Detector with default settings, Feature Mapper, and Precursor Ions Quantifier nodes within the Proteome Discoverer. In Feature Mapper module, retention time (RT) alignment was performed across raw files, allowing a maximum RT shift of 2 min. In the Precursor Ions Quantifier node, precursor abundance was calculated based on area, and normalization was performed using the total peptide amount per raw file. Protein abundance was derived by summing the abundances of unique peptides assigned to each protein.

Data analysis

All quantitative data are shown as means ± SEM unless otherwise indicated. Statistical differences between two groups were analyzed using a two-tailed Student's *t* test. Significant differences among three or more groups were also analyzed by analysis of variance (ANOVA) with Bonferroni's post hoc analysis. The results were considered significant when the *P* value was less than 0.05.

Supplementary Materials

This PDF file includes:

Figs. S1 to S15

Table S1

REFERENCES

1. D. Walter, A. Lier, A. Geiselhart, F. B. Thalheimer, S. Huntscha, M. C. Sobotta, B. Moehrle, D. Brocks, I. Bayindir, P. Kaschutnig, K. Muedder, C. Klein, A. Jauch, T. Schroeder, H. Geiger, T. P. Dick, T. Holland-Letz, P. Schmezer, S. W. Lane, M. A. Rieger, M. A. Essers, D. A. Williams, A. Trumpp, M. D. Milsom, Exit from dormancy provokes DNA-damage-induced attrition in haematopoietic stem cells. *Nature* **520**, 549–552 (2015).
2. A. Wilson, E. Laurenti, G. Oser, R. C. van der Wath, W. Blanco-Bose, M. Jaworski, S. Offner, C. F. Dunant, L. Eshkind, E. Bockamp, P. Lio, H. R. Macdonald, A. Trumpp, Hematopoietic stem cells reversibly switch from dormancy to self-renewal during homeostasis and repair. *Cell* **135**, 1118–1129 (2008).
3. G. Guenechea, O. I. Gan, C. Dorrell, J. E. Dick, Distinct classes of human stem cells that differ in proliferative and self-renewal potential. *Nat. Immunol.* **2**, 75–82 (2001).
4. A. Trumpp, M. Essers, A. Wilson, Awakening dormant haematopoietic stem cells. *Nat. Rev. Immunol.* **10**, 201–209 (2010).
5. S. Pinho, P. Frenette, Haematopoietic stem cell activity and interactions with the niche. *Nat. Rev. Mol. Cell Biol.* **20**, 303–320 (2019).
6. M. J. Kiel, O. H. Yilmaz, T. Iwashita, O. H. Yilmaz, C. Terhorst, S. J. Morrison, SLAM family receptors distinguish hematopoietic stem and progenitor cells and reveal endothelial niches for stem cells. *Cell* **121**, 1109–1121 (2005).
7. Y. Kunisaki, I. Bruns, C. Scheiermann, J. Ahmed, S. Pinho, D. Zhang, T. Mizoguchi, Q. Wei, D. Lucas, K. Ito, J. C. Mar, A. Bergman, P. S. Frenette, Arteriolar niches maintain haematopoietic stem cell quiescence. *Nature* **502**, 637–643 (2013).
8. S. Mendez-Ferrer, T. V. Michurina, F. Ferraro, A. R. Mazloom, B. D. Macarthur, S. A. Lira, D. T. Scadden, A. Ma'ayan, G. N. Enikolopov, P. S. Frenette, Mesenchymal and haematopoietic stem cells form a unique bone marrow niche. *Nature* **466**, 829–834 (2010).
9. L. Ding, T. L. Saunders, G. Enikolopov, S. J. Morrison, Endothelial and perivascular cells maintain haematopoietic stem cells. *Nature* **481**, 457–462 (2012).
10. A. Greenbaum, Y. M. Hsu, R. B. Day, L. G. Schuettpelz, M. J. Christopher, J. N. Borgerding, T. Nagasawa, D. C. Link, CXCL12 in early mesenchymal progenitors is required for haematopoietic stem-cell maintenance. *Nature* **495**, 227–230 (2013).
11. B. O. Zhou, R. Yue, M. M. Murphy, J. G. Peyer, S. J. Morrison, Leptin-receptor-expressing mesenchymal stromal cells represent the main source of bone formed by adult bone marrow. *Cell Stem Cell* **15**, 154–168 (2014).
12. J. A. Kim, J. S. Shim, G. Y. Lee, H. W. Yim, T. M. Kim, M. Kim, S. H. Leem, J. W. Lee, C. K. Min, I. H. Oh, Microenvironmental remodeling as a parameter and prognostic factor of heterogeneous leukemogenesis in acute myelogenous leukemia. *Cancer Res.* **75**, 2222–2231 (2015).
13. K. Schepers, E. M. Pietras, D. Reynaud, J. Flach, M. Binnewies, T. Garg, A. J. Wagers, E. C. Hsiao, E. Passegue, Myeloproliferative neoplasia remodels the endosteal bone marrow niche into a self-reinforcing leukemic niche. *Cell Stem Cell* **13**, 285–299 (2013).
14. L. Arranz, A. Sanchez-Aguilera, D. Martin-Perez, J. Isern, X. Langa, A. Tzankov, P. Lundberg, S. Muntion, Y. S. Tzeng, D. M. Lai, J. Schwaller, R. C. Skoda, S. Mendez-Ferrer, Neuropathy of haematopoietic stem cell niche is essential for myeloproliferative neoplasms. *Nature* **512**, 78–81 (2014).
15. M. Hanoun, D. Zhang, T. Mizoguchi, S. Pinho, H. Pierce, Y. Kunisaki, J. Lacombe, S. A. Armstrong, U. Duhrsen, P. S. Frenette, Acute myelogenous leukemia-induced sympathetic neuropathy promotes malignancy in an altered hematopoietic stem cell niche. *Cell Stem Cell* **15**, 365–375 (2014).
16. S. Y. Jeong, J. A. Kim, I. H. Oh, The adaptive remodeling of stem cell niche in stimulated bone marrow counteracts the leukemic niche. *Stem Cells* **36**, 1617–1629 (2018).
17. J. H. Kim, H. S. Lee, H. K. Choi, J. A. Kim, I. S. Chu, S. H. Leem, I. H. Oh, Heterogeneous niche activity of ex-vivo expanded MSCs as factor for variable outcomes in hematopoietic recovery. *PLOS ONE* **11**, e0168036 (2016).
18. C. R. Walkley, J. M. Shea, N. A. Sims, L. E. Purton, S. H. Orkin, Rb regulates interactions between hematopoietic stem cells and their bone marrow microenvironment. *Cell* **129**, 1081–1095 (2007).
19. K. R. Kwon, J. Y. Ahn, M. S. Kim, J. Y. Jung, J. H. Lee, I. H. Oh, Disruption of bis leads to the deterioration of the vascular niche for hematopoietic stem cells. *Stem Cells* **28**, 268–278 (2010).
20. Y. Omatsu, M. Seike, T. Sugiyama, T. Kume, T. Nagasawa, Foxc1 is a critical regulator of haematopoietic stem/progenitor cell niche formation. *Nature* **508**, 536–540 (2014).
21. F. Nakahara, D. K. Borger, Q. Wei, S. Pinho, M. Maryanovich, A. H. Zahalka, M. Suzuki, C. D. Cruz, Z. Wang, C. Xu, P. E. Boulais, A. Ma'ayan, J. M. Greally, P. S. Frenette, Engineering a haematopoietic stem cell niche by revitalizing mesenchymal stromal cells. *Nat. Cell Biol.* **21**, 560–567 (2019).
22. S. Jeon, H.-S. Lee, G.-Y. Lee, G. Park, T.-M. Kim, J. Shin, C. Lee, I.-H. Oh, Shift of EMT gradient in 3D spheroid MSCs for activation of mesenchymal niche function. *Sci. Rep.* **7**, 6859 (2017).
23. J. Isern, A. Garcia-Garcia, A. M. Martin, L. Arranz, D. Martin-Perez, C. Torroja, F. Sanchez-Cabo, S. Mendez-Ferrer, The neural crest is a source of mesenchymal stem cells with specialized hematopoietic stem cell niche function. *eLife* **3**, e03696 (2014).
24. M. Zhao, L. Kong, Y. Liu, H. Qu, dbEMT: An epithelial-mesenchymal transition associated gene resource. *Sci. Rep.* **5**, 11459 (2015).
25. S. Lamouille, J. Xu, R. Derynck, Molecular mechanisms of epithelial-mesenchymal transition. *Nat. Rev. Mol. Cell Biol.* **15**, 178–196 (2014).
26. J. Zhang, C. Niu, L. Ye, H. Huang, X. He, W. G. Tong, J. Ross, J. Haug, T. Johnson, J. Q. Feng, S. Harris, L. M. Wiedemann, Y. Mishina, L. Li, Identification of the haematopoietic stem cell niche and control of the niche size. *Nature* **425**, 836–841 (2003).
27. Y. S. An, E. Lee, M. H. Kang, H. S. Hong, M. R. Kim, W. S. Jang, Y. Son, J. Y. Yi, Substance P stimulates the recovery of bone marrow after the irradiation. *J. Cell. Physiol.* **226**, 1204–1213 (2011).
28. H. S. Hong, S. Kim, Y. Jin, Y. Son, Substance P enhances the therapeutic effect of MSCs by modulating their angiogenic potential. *J. Cell Mol. Med.* **24**, 12560–12571 (2020).
29. B. Peault, I. L. Weissman, A. M. Buckle, A. Tsukamoto, C. Baum, Thy-1-expressing CD34+ human cells express multiple hematopoietic potentialities in vitro and in SCID-hu mice. *Nouv. Rev. Fr. Hematol.* **35**, 91–93 (1993).
30. D. Sa da Bandeira, J. Casamitjana, M. Crisan, Pericytes, integral components of adult hematopoietic stem cell niches. *Pharmacol. Ther.* **171**, 104–113 (2017).
31. B. Zhang, Y. W. Ho, Q. Huang, T. Maeda, A. Lin, S. U. Lee, A. Hair, T. L. Holyoake, C. Huettner, R. Bhatia, Altered microenvironmental regulation of leukemic and normal stem cells in chronic myelogenous leukemia. *Cancer Cell* **21**, 577–592 (2012).
32. E. A. Clark, S. Kalomoiris, J. A. Nolta, F. A. Fierro, Concise review: MicroRNA function in multipotent mesenchymal stromal cells. *Stem Cells* **32**, 1074–1082 (2014).
33. J. Zhang, H. Y. Jin, Y. Wu, Z. C. Zheng, S. Guo, Y. Wang, D. Yang, X. Y. Meng, X. Xu, Y. Zhao, Hypoxia-induced LncRNA PCGEM1 promotes invasion and metastasis of gastric cancer through regulating SNAI1. *Clin. Transl. Oncol.* **21**, 1142–1151 (2019).
34. D. J. Ceradini, G. C. Gurtner, Homing to hypoxia: HIF-1 as a mediator of progenitor cell recruitment to injured tissue. *Trends Cardiovasc. Med.* **15**, 57–63 (2005).
35. J. A. Morales-González, E. Madrigal-Santillán, Á. Morales-González, M. Bautista, E. Gayosso-Islas, C. Sánchez-Moreno, What is known regarding the participation of factor Nrf-2 in liver regeneration? *Cells* **4**, 169–177 (2015).
36. I. Fioroni, E. Dell'Aquila, F. Pantano, S. Intagliata, M. Caricato, B. Vincenzi, R. Coppola, D. Santini, G. Tonini, Role of c-mesenchymal-epithelial transition pathway in gastric cancer. *Expert Opin. Pharmacother.* **16**, 1195–1207 (2015).
37. Y. Zhou, J. Xu, Y. Liu, J. Li, C. Chang, C. Xu, Rat hepatocytes weighted gene co-expression network analysis identifies specific modules and hub genes related to liver regeneration after partial hepatectomy. *PLOS ONE* **9**, e94868 (2014).
38. L. Xie, Y. Yin, L. Benowitz, Chemokine CCL5 promotes robust optic nerve regeneration and mediates many of the effects of CNTF gene therapy. *Proc. Natl. Acad. Sci. U.S.A.* **118**, e2017282118 (2021).
39. M. Deng, Y. Hou, J. Liu, J. He, Z. Lan, H. Xiao, Mesenchymal stem cell-derived exosomes overexpressing SRC-3 protect mice from cerebral ischemia by inhibiting ferroptosis. *Brain Res. Bull.* **211**, 110948 (2024).
40. D. Jing, C. Li, K. Yao, X. Xie, P. Wang, H. Zhao, J. Q. Feng, Z. Zhao, Y. Wu, J. Wang, The vital role of Gli1^{+} mesenchymal stem cells in tissue development and homeostasis. *J. Cell. Physiol.* **236**, 6077–6089 (2021).
41. Y. Luo, S. Ge, Q. Chen, S. Lin, W. He, M. Zeng, Overexpression of FoxM1 optimizes the therapeutic effect of bone marrow mesenchymal stem cells on acute respiratory distress syndrome. *Stem Cell Res. Ther.* **14**, 27 (2023).
42. Y. Luo, S. Lin, X. Mao, Y. Yang, W. He, M. Guo, M. Zeng, Overexpression of FoxM1 enhanced the protective effect of bone marrow-derived mesenchymal stem cells on lipopolysaccharide-induced acute lung injury through the activation of Wnt/β-catenin signaling. *Oxid. Med. Cell. Longev.* **2023**, 8324504 (2023).
43. F. Rehfeld, A. M. Rohde, D. T. Nguyen, F. G. Wulczyn, Lin28 and let-7: Ancient milestones on the road from pluripotency to neurogenesis. *Cell Tissue Res.* **359**, 145–160 (2015).
44. Z. Ding, J. Lin, Y. Sun, S. Cong, S. Liu, Y. Zhang, Q. Chen, J. Chen, miR-122-5p negatively regulates the transforming growth factor-β/Smad signaling pathway in skeletal muscle myogenesis. *Cell Biochem. Funct.* **38**, 231–238 (2020).
45. S. Hünten, H. Hermeking, p53 directly activates cystatin D/CST5 to mediate mesenchymal-epithelial transition: a possible link to tumor suppression by vitamin D3. *Oncotarget* **6**, 15842–15856 (2015).
46. S. J. Szilvassy, R. K. Humphries, P. M. Lansdorp, A. C. Eaves, C. J. Eaves, Quantitative assay for totipotent reconstituting hematopoietic stem cells by a competitive repopulation strategy. *Proc. Natl. Acad. Sci. U.S.A.* **87**, 8736–8740 (1990).
47. M. Crisan, S. Yap, L. Casteilla, C. W. Chen, M. Corselli, T. S. Park, G. Andriolo, B. Sun, B. Zheng, L. Zhang, C. Norotte, P. N. Teng, J. Traas, R. Schugar, B. M. Deasy, S. Badylak, H. J. Buhring, J. P. Giacobino, L. Lazzari, J. Huard, B. Peault, A perivascular origin for mesenchymal stem cells in multiple human organs. *Cell Stem Cell* **3**, 301–313 (2008).
48. A. Kaminska, K. Radoszkiewicz, P. Rybkowska, A. Wedzinska, A. Sarnowska, Interaction of neural stem cells (NSCs) and mesenchymal stem cells (MSCs) as a promising approach in brain study and nerve regeneration. *Cells* **11**, 1464 (2022).

49. K. Park, H. Heo, M. E. Han, K. Choi, J. H. Yi, S. J. Kang, Y. K. Kwon, K. S. Shin, Learning-induced synaptic potentiation in implanted neural precursor cell-derived neurons. *Sci. Rep.* **5**, 17796 (2015).
50. J. T. Gonçalves, S. T. Schafer, F. H. Gage, Adult neurogenesis in the hippocampus: From stem cells to behavior. *Cell* **167**, 897–914 (2016).
51. R. O. Soares, D. M. Losada, M. C. Jordani, P. Évora, O. Castro-e-Silva, Ischemia/reperfusion injury revisited: An overview of the latest pharmacological strategies. *Int. J. Mol. Sci.* **20**, 5034 (2019).
52. Y. Kfoury, D. T. Scadden, Mesenchymal cell contributions to the stem cell niche. *Cell Stem Cell* **16**, 239–253 (2015).
53. M. Krampera, K. Le Blanc, Mesenchymal stromal cells: Putative microenvironmental modulators become cell therapy. *Cell Stem Cell* **28**, 1708–1725 (2021).
54. A. I. Caplan, D. Correa, The MSC: an injury drugstore. *Cell Stem Cell* **9**, 11–15 (2011).
55. O. Levy, R. Kuai, E. M. J. Siren, D. Bhere, Y. Milton, N. Nissar, M. De Biasio, M. Heinelt, B. Reeve, R. Abdi, M. Alturki, M. Fallatah, A. Almalik, A. H. Alhasan, K. Shah, J. M. Karp, Shattering barriers toward clinically meaningful MSC therapies. *Sci. Adv.* **6**, eaba6884 (2020).
56. E. Forte, F. Miraldi, I. Chimenti, F. Angelini, A. Zeuner, A. Giacomello, M. Mercola, E. Messina, TGFβ-dependent epithelial-to-mesenchymal transition is required to generate cardiospheres from human adult heart biopsies. *Stem Cells Dev.* **21**, 3081–3090 (2012).
57. C. E. Weber, N. Y. Li, P. Y. Wai, P. C. Kuo, Epithelial-mesenchymal transition, TGF-beta, and osteopontin in wound healing and tissue remodeling after injury. *J. Burn Care Res.* **33**, 311–318 (2012).
58. Q. Wei, F. Nakahara, N. Asada, D. Zhang, X. Gao, C. Xu, A. Alfieri, N. P. Brodin, S. E. Zimmerman, J. C. Mar, C. Guha, W. Guo, P. S. Frenette, Snai2 maintains bone marrow niche cells by repressing osteopontin expression. *Dev. Cell* **53**, 503–513.e5 (2020).
59. Y. Atlasi, H. G. Stunnenberg, The interplay of epigenetic marks during stem cell differentiation and development. *Nat. Rev. Genet.* **18**, 643–658 (2017).
60. Y. S. Chung, H. J. Kim, T. M. Kim, S. H. Hong, K. R. Kwon, S. An, J. H. Park, S. Lee, I. H. Oh, Undifferentiated hematopoietic cells are characterized by a genome-wide undermethylation dip around the transcription start site and a hierarchical epigenetic plasticity. *Blood* **114**, 4968–4978 (2009).
61. S. A. Mani, W. Guo, M. J. Liao, E. N. Eaton, A. Ayyanan, A. Y. Zhou, M. Brooks, F. Reinhard, C. C. Zhang, M. Shipitsin, L. L. Campbell, K. Polyak, C. Brisken, J. Yang, R. A. Weinberg, The epithelial-mesenchymal transition generates cells with properties of stem cells. *Cell* **133**, 704–715 (2008).
62. C. D. May, N. Sphyris, K. W. Evans, S. J. Werden, W. Guo, S. A. Mani, Epithelial-mesenchymal transition and cancer stem cells: A dangerously dynamic duo in breast cancer progression. *Breast Cancer Res.* **13**, 202 (2011).
63. X. Ye, W. L. Tam, T. Shibue, Y. Kaygusuz, F. Reinhardt, E. Ng Eaton, R. A. Weinberg, Distinct EMT programs control normal mammary stem cells and tumour-initiating cells. *Nature* **525**, 256–260 (2015).
64. R. Kalluri, R. A. Weinberg, The basics of epithelial-mesenchymal transition. *J. Clin. Investig.* **119**, 1420–1428 (2009).
65. G. Mangialardi, A. Cordaro, P. Madeddu, The bone marrow pericyte: An orchestrator of vascular niche. *Regen. Med.* **11**, 883–895 (2016).
66. C. F. Hung, S. Holton, Y. H. Chow, W. C. Liles, S. A. Gharib, W. A. Altemeier, Pericyte-like cells undergo transcriptional reprogramming and distinct functional adaptations in acute lung injury. *FASEB J.* **35**, e21323 (2021).
67. H. R. Lee, S. Kim, S. Shin, S. Y. Jeong, D. W. Lee, S. U. Lim, J. Y. Kang, M. Y. Son, C. Lee, K. R. Yu, M. Kim, I. H. Oh, iPSC-derived MSCs are a distinct entity of MSCs with higher therapeutic potential than their donor-matched parental MSCs. *Int. J. Mol. Sci.* **24**, 881 (2023).
68. V. Giudice, C. Selleri, Aplastic anemia: Pathophysiology. *Semin. Hematol.* **59**, 13–20 (2022).
69. K. Aomatsu, T. Arao, K. Abe, A. Kodama, K. Sugioka, K. Matsumoto, K. Kudo, H. Kimura, Y. Fujita, H. Hayashi, T. Nagai, Y. Shimomura, K. Nishio, Slug is upregulated during wound healing and regulates cellular phenotypes in corneal epithelial cells. *Invest. Ophthalmol. Vis. Sci.* **53**, 751–756 (2012).
70. B. Hotz, A. Visekruna, H. J. Buhr, H. G. Hotz, Beyond epithelial to mesenchymal transition: a novel role for the transcription factor Snail in inflammation and wound healing. *J. Gastrointest. Surg.* **14**, 388–397 (2010).
71. G. Swetha, V. Chandra, S. Phadnis, R. Bhonde, Glomerular parietal epithelial cells of adult murine kidney undergo EMT to generate cells with traits of renal progenitors. *J. Cell. Mol. Med.* **15**, 396–413 (2011).
72. K. Janeczek Portalska, A. Leferink, N. Groen, H. Fernandes, L. Moroni, C. van Blitterswijk, J. de Boer, Endothelial differentiation of mesenchymal stromal cells. *PLOS ONE* **7**, e46842 (2012).
73. O. Vittorio, E. Jacchetti, S. Pacini, M. Cecchini, Endothelial differentiation of mesenchymal stromal cells: when traditional biology meets mechanotransduction. *Integr. Biol.* **5**, 291–299 (2013).

Acknowledgments: This research was supported by the ABC-based Regenerative BioTherapeutics (ABC project) grant to I.-H.O. funded by the Korean government (the Ministry of Health and Welfare) (RS-2024-00465298) and, in part, by National Research Foundation of Korea (NRF) grant to H.-J.P. funded by the Korean government (MSIT) (RS-2024-00440285). **Funding:** The ABC-based Regenerative BioTherapeutics (ABC project) grant to I.-H.O. funded by the Korean government (the Ministry of Health and Welfare) (RS-2024-00465298). The National Research Foundation of Korea (NRF) grants to H.-J.P. funded by the Korean government, the Ministry of Science and ICT (MSIT) (RS-2024-00440285). **Author contributions:** Experiment and generated data: J.-A.K., B.-W.P., H.-R.L., G.-A.J., S.L., W.-S.S., H.L., Y.-J.K., and J.K. Proteomics analysis: S.S. and C.L. Research on clinical study for AA and leukemia: S.P., J.-W.L., and H.-J.K. Designed the study and supervision: I.-H.O., Y.K.K., and H.-J.P. Writing—original draft: I.-H.O. Writing—review and editing: I.-H.O., H.-J.K., Y.K.K., and H.-J.P. **Competing interests:** I.-H.O. is the founder of RegenInnopharm Inc. The other authors declare that they have no competing interests. **Data and materials availability:** All data and code needed to evaluate and reproduce the results in the paper are present in the paper and/or the Supplementary Materials.

Submitted 13 May 2025
Accepted 21 November 2025
Published 1 January 2026
10.1126/sciadv.ady9664